Nano Research

Open Access

Research Article

Customizable topological neuro-mimetic hydrogels based on mechanical training for functional recovery following peripheral nerve injury

Xueying Hou[1,2,§], Zong Chen[3,4,§], Enchong Zhang[5,§], Yukun Mao[6], Zhiwei Fan[7], Xiaodan Sun[8,9] ✉, Chunlin Liu[7,10] ✉, and Anhua Wu[1,2] ✉

[1] *Department of Neurosurgery, Shengjing Hospital of China Medical University, Shenyang 110004, China*
[2] *Institute of Health Sciences, China Medical University, Shenyang 110134, China*
[3] *Department of Plastic and Aesthetic Surgery, Peking Union Medical College Hospital, Chinese Academy of Medical Sciences and Peking Union Medical College, Beijing 100730, China*
[4] *Center for Regenerative Medicine & Plastic Surgery Research, Peking Union Medical College Hospital, Beijing 100730, China*
[5] *Department of Urology, Shengjing Hospital of China Medical University, Shenyang 110004, China*
[6] *Plastic Surgery Hospital, Chinese Academy of Medical Sciences and Peking Union Medical College, Beijing 100144, China*
[7] *School of Mechanical Engineering, Chengdu University, Chengdu 610000, China*
[8] *Key Laboratory of New Ceramics and Fine Processing, School of Materials Science and Engineering, Tsinghua University, Beijing 100084, China*
[9] *Developmental BioEngineering Group, TechMed Center, University of Twente, 7500 AE Enschede, the Netherlands*
[10] *Tianfu Jiangxi Laboratory, Chengdu 641419, China*
[§] *Xueying Hou, Zong Chen, and Enchong Zhang contributed equally to this work.*

Cite this article: *Nano Research*, **2026**, *19*, 94908570. https://doi.org/10.26599/NR.2026.94908570

ABSTRACT: After peripheral nerve injury, nerve guidance conduits (NGCs) offer an effective alternative to autologous nerve grafting for repairing nerve defects. However, without a well-defined topological structure, peripheral nerve regeneration often results in disorganized growth. Because the regeneration site is subject to bodily movement, the conduits must possess sufficient mechanical integrity to function within this dynamic environment. We prepared double-network hydrogel films from polyvinyl alcohol (PVA) and gelatin for nerve regeneration applications. Using freeze-thaw crystallization, the Hofmeister effect, borate bonding, and incorporating poly(3,4-ethylenedioxythiophene): polystyrene sulfonate (PEDOT:PSS), along with continuous optimization of the formulation, the hydrogel achieved excellent mechanical properties. With repeated mechanical training, the hydrogel surface developed a fibrous-like topological structure and could also carry and gradually release nerve growth factor (NGF). The hydrogel could be shaped by cutting and origami folding, and was then firmly attached to the nerve defect via chitosan stitching adhesives, providing a foundation for nerve regeneration. The conduit exhibited a degradation rate closely matching the nerve regeneration process and excellent biocompatibility, while also promoting the oriented growth and differentiation of PC12 cells. *In vivo* evaluation in a rat sciatic nerve defect model demonstrated that the conduit suppressed inflammation, activated calcium signaling and PPAR pathways in the early regenerative phase, and promoted axon regeneration, remyelination, and functional recovery.

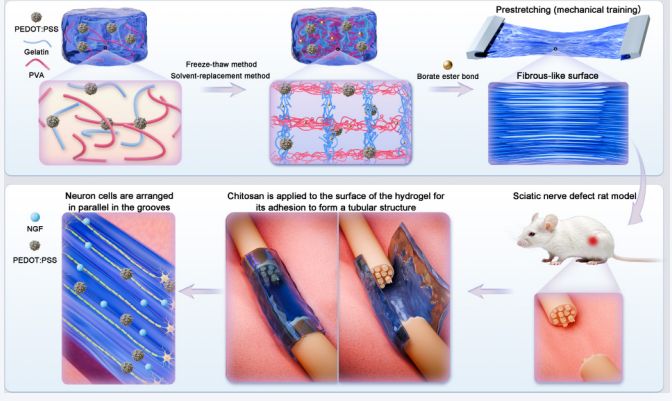

KEYWORDS: mechanical training, double-network hydrogel, surface topography, nerve guidance conduit

Received: November 20, 2025; **Revised:** February 6, 2026
Accepted: February 13, 2026

✉Address correspondence to Xiaodan Sun, sunxiaodan@tsinghua.edu.cn; Chunlin Liu, liuchunlin@cdu.edu.cn; Anhua Wu, ahwu@cmu.edu.cn

1 Introduction

Peripheral nerves are fragile and highly susceptible to injury from trauma, iatrogenic interventions, or disease. Such damage, clinically termed peripheral nerve injury (PNI), disrupts the structural and

functional integrity of the nerves, impairing the brain's communication with muscles and organs. This disruption leads to severe sensory, motor, and autonomic deficits, significantly compromising a patient's quality of life [1]. Currently, autologous nerve grafting remains the gold standard for the treatment of PNI [2, 3]. However, this approach is associated with significant drawbacks, primarily the necessity of harvesting healthy nerve tissue from the patient's own body. This procedure not only causes secondary damage at the donor site but also carries the risk of various complications, including mismatched nerve fascicles, sensory loss in the donor area, and neuroma formation [4–6]. These limitations have motivated extensive research into alternative strategies, particularly the development of artificial nerve guidance conduits (NGCs) that can bypass the need for autografts [2]. Among these, hydrogel-based NGCs have emerged as a promising platform due to their biomimetic properties, and tunable physical and biochemical characteristics. An effective nerve guidance conduit should meet several key requirements: it must be biocompatible, biodegradable, mechanically supportive of regenerating nerves, flexible, and capable of providing physiological cues for nerve regeneration [2]. Due to the presence of specific microstructures and the ability to trigger biochemical signals, hydrogel surfaces can closely replicate the characteristics of the extracellular matrix, offering structural support and signaling cues that facilitate cell proliferation, polarization, differentiation, and organized tissue formation. Consequently, micropatterned designs that guide cellular alignment have attracted considerable research interest [7, 8].

Currently, several studies have developed NGCs featuring internal microgrooves, which have been shown to promote oriented growth of nerve cells. However, the fabrication of such grooved conduits often relies on high-precision 3D printing, electrospinning, or intricate molding techniques—approaches that involve complex manufacturing processes, exhibit poor mechanical strength, and entail high production costs [2, 9]. For instance, while electrospinning can produce highly aligned nanofibers, the resulting scaffolds often suffer from limited mechanical robustness and low yield, typically requiring a labor-intensive two-step process that involves inserting the scaffold into an external supporting tube [10, 11]. Moreover, as research in this field advances, there is a growing demand for NGCs that not only possess adequate mechanical properties but are also capable of incorporating bioactive components or therapeutic agents [2]. Therefore, there remains an urgent need to develop innovative manufacturing strategies that address these limitations. In this context, topographical engineering via "mechanical training" emerges as a compelling alternative. This approach typically involves the programmed stretching of pre-formed hydrogels to induce bulk alignment of their internal polymer networks [12, 13], thereby directly creating topographies without relying on complex material deposition or expensive tooling. Compared to the aforementioned techniques, mechanical training offers distinct advantages: (i) It enhances the intrinsic mechanical properties of the conduit material by promoting molecular alignment and densification [12], addressing the common issue of scaffold fragility; and (ii) it represents a simpler and potentially more cost-effective post-processing step applicable to a wide range of hydrogel systems that already serve as versatile platforms for bioactive integration [13]. Consequently, this method provides a direct route for overcoming the key limitations of mechanical weakness, complex processing, and high cost associated with the traditional fabrication of grooved NGCs.

In this study, we presented a customizable topological nerve conduit inspired by mechanical training (Fig. 1). We first developed a dual-network composite hydrogel based on polyvinyl alcohol (PVA) and gelatin. By combining freeze-thaw cycles, immersion in ammonium sulfate solution to utilize the Hofmeister effect, and dynamic regulation through borate ester bonding, the mechanical properties of the hydrogel were comprehensively optimized. The resulting PVA/gelatin/boric acid/ammonium sulfate (PGBA) hydrogel exhibited excellent mechanical support, stretchability, anti-swelling capacity, and adaptability to compressive stress *in vivo*,

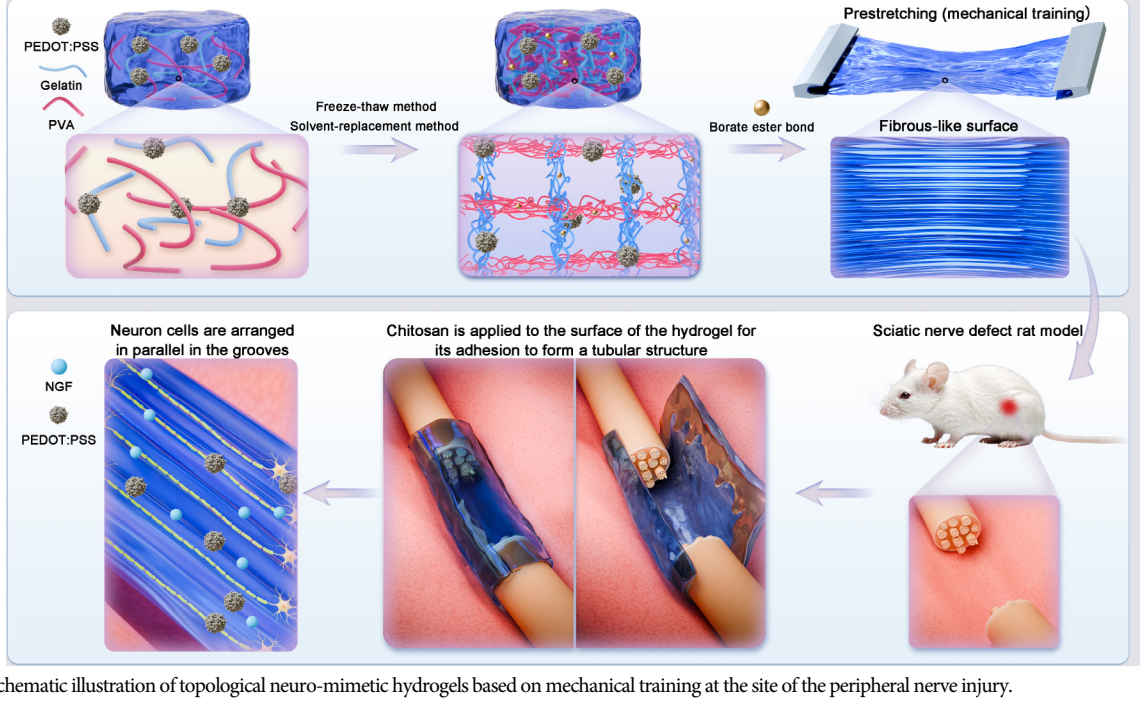

Figure 1 Schematic illustration of topological neuro-mimetic hydrogels based on mechanical training at the site of the peripheral nerve injury.

demonstrating excellent integrated performance. Some studies have highlighted the promising role of poly(3,4-ethylenedioxythiophene): polystyrene sulfonate (PEDOT:PSS) in PNI repair [14, 15]. In this study, PEDOT:PSS was incorporated into a PGBA hydrogel (referred to as PGBAP) to increase its electrical conductivity. Through repeated mechanical training, the original surface architecture of the composite hydrogel underwent controlled disruption, followed by the reconstruction of fibrous-like surface topographies. These engineered surface features provide topographical cues that can promote the aligned growth of neural cells, thereby enhancing guided nerve regeneration. Inspired by origami, the hydrogel was cut and manually folded into a tubular conduit and then sealed with a stitching adhesive. The hydrogel we developed can be loaded with bioactive components such as nerve growth factor (NGF) to achieve sustained release, and mechanistically, this strategy modulates the early regenerative microenvironment by suppressing inflammation, activating calcium signaling and PPAR pathways, and attenuating cellular senescence and apoptosis. By orchestrating these molecular and cellular events, it establishes a pro-regenerative niche that holds significant potential for improving clinical outcomes in peripheral nerve repair. This approach integrates topographical, mechanical, and electrical cues, allowing more precise customization for different nerve injury scenarios through their synergistic effects.

2 Results and discussion

2.1 Design strategy for the PGBA hydrogels

The strategy for preparing PGBA is shown in Fig. S1 in the Electronic Supplementary Material (ESM). After undergoing freeze-thaw treatment, PVA chains aggregate at low temperatures and form crystalline regions via hydrogen bonding. These crystalline domains serve as physical crosslinking points, significantly enhancing the mechanical strength and structural stability of the hydrogel. After immersing the hydrogel in an ammonium sulfate solution, its Hofmeister effect could be used to induce enhanced hydrophobic and ionic interactions, leading to a denser and more compact structure of PVA and gelatin. The ammonium sulfate ions significantly strengthen the hydrophobic interactions and chain bundling within the gelatin network. The physical crosslinking introduced via the Hofmeister effect allows rapid energy absorption and enables the hydrogel to withstand large deformations through reversible decrosslinking and dissociation, thereby imparting excellent energy dissipation and antifatigue properties [13, 16]. The addition of boric acid enables the formation of boronic ester bonds through interactions with hydroxyl groups. These boronic ester bonds establish a dynamic network within the hydrogel, which improves the structural compactness and provides resistance against swelling. This bond is formed through reactions between diol-containing polymers, such as PVA, and boric acid or its derivatives. The resulting boronic ester bonds can undergo rapid dissociation and reformation under ambient conditions without the need for catalysts or external stimuli [17, 18].

2.2 Mechanical properties

Previous NGCs often suffered mechanical failure during long-term repair because of repeated mechanical deformation after implantation. Therefore, NGCs must possess sufficient mechanical strength and stability to provide a consistent and supportive environment for nerve regeneration [19, 20]. Uniaxial tensile, cyclic tensile, and compression tests were conducted to evaluate the mechanical properties of hydrogels. As shown in Figs. 2(a)–2(k), uniaxial tensile tests were performed to analyze the effects of the concentrations of different components, including PVA, gelatin, boric acid, and ammonium sulfate, on the mechanical performance of the hydrogels. Based on the measurements of fracture elongation and tensile strength, the optimal formulation was preliminarily determined. The PGBAP hydrogel exhibited a maximum elongation at break of 299.81% ± 13.90% and a tensile strength of 2.14 ± 0.17 MPa when prepared with 10 wt.% PVA, 10 wt.% gelatin, 0.04 mol/L boric acid, and 20 wt.% ammonium sulfates.

The incorporation of boric acid and ammonium sulfate significantly increased the mechanical performance of the hydrogel [21]. The formation of dynamic borate ester bonds imparted excellent stretchability to the hydrogel, whereas the Hofmeister effect promoted an increase in Young's modulus. Following the incorporation of the nano-conductive material PEDOT:PSS, the electrical conductivity of the hydrogel increased significantly (Fig. S2 in the ESM). The π-electron delocalization in the conjugated backbone of PGBAP hydrogel facilitated efficient electronic conductivity, which closely mimicked the native electrical behavior of neuronal tissue, thus supporting the regeneration and functional reconnection of damaged nerves [22, 23]. Compared with the PGAP hydrogel, the mean elongation at break, tensile strength, and Young's modulus of the PGBAP hydrogel increased by 170.42%, 162.12%, and 507.87%, respectively (Figs. 2(j) and 2(k), and Fig. S3 in the ESM), suggesting markedly enhanced elasticity. The compressive modulus was about 72.32 ± 10.23 kPa (Fig. S6 in the ESM). These enhancements also provided robust mechanical support for subsequent pre-stretching processes (Video S1 in the ESM).

The fatigue resistance of the hydrogel after 0, 100, 500, and 800 consecutive loading-unloading cycles is shown in Fig. S4 in the ESM. There was a recovery period of 1 min between each cycle, indicating its suitability for use in nerve conduits. The hysteresis loops of the PGBAP hydrogel nearly overlapped throughout repeated cycles, and a hysteresis ratio exceeding 97% was maintained even after 800 cycles, which indicated excellent fatigue resistance (Fig. S5 in the ESM). Strong fatigue resistance allows nerve conduits to endure repeated mechanical stress in the body without failure, ensuring consistent structural support for nerve regeneration.

After implantation, the material should provide structural support and protection to the injured peripheral nerves, and its slow degradation rate prevents compression of the newly regenerated nerve fibers [24]. Its compressive properties were further evaluated, and the hydrogel withstood compressive strains ranging from 10% to 30% without experiencing structural failure (Fig. 2(l)).

2.3 Strategy for topological adhesion via polymer stitching

The PGBAP hydrogel exhibited a certain degree of inherent adhesiveness; however, it could not form a robust adhesive layer. To address this issue, we adopted a strategy inspired by Suo et al. [25, 26], in which a layer of chitosan solution was applied to the surface of the hydrogel. This solution diffuses into the hydrogel matrix, thereby forming a strong interfacial bonding layer. As shown in Fig. 2(m), both the hydrogel matrix and surrounding

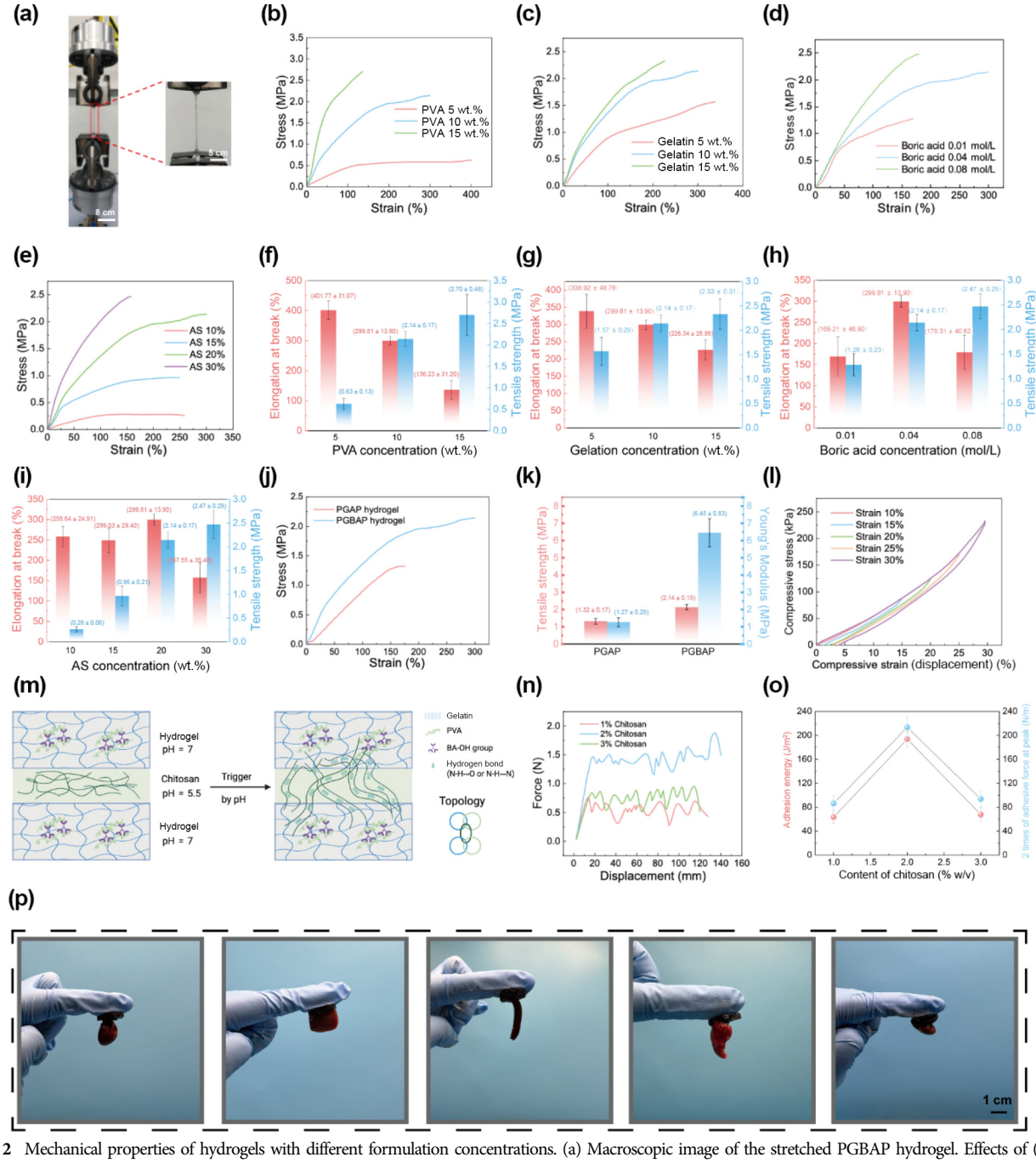

Figure 2 Mechanical properties of hydrogels with different formulation concentrations. (a) Macroscopic image of the stretched PGBAP hydrogel. Effects of (b) PVA content (5 wt.%, 10 wt.%, and 15 wt.%), (c) gelatin content (5 wt.%, 10 wt.%, and 15 wt.%), (d) boric acid concentration (0.01, 0.04, and 0.08 mol/L), and (e) ammonium sulfate content (10 wt.%, 15 wt.%, 20 wt.%, and 30 wt.%) on tensile stress-strain behavior. Effects of (f) PVA content (5 wt.%, 10 wt.%, and 15 wt.%), (g) gelatin content (5 wt.%, 10 wt.%, and 15 wt.%), (h) boric acid concentration (0.01, 0.04, and 0.08 mol/L), and (i) ammonium sulfate content (10 wt.%, 15 wt.%, 20 wt.%, and 30 wt.%) on elongation at break and tensile strength of the PGAP hydrogel. (j) and (k) Tensile stress-strain curves and corresponding Young's moduli of the PGAP and PGBAP hydrogels. Compressive stress-strain curve of the PGBAP hydrogel under 30% strain. (m) Schematic illustration of the mechanism by which chitosan stitches polymers. (n) Representative force-displacement curve of the PGBAP hydrogel during the T-peel test. (o) Adhesion energy and the two-fold increase in peak adhesion force per unit width of PGBAP hydrogels coated with chitosan adhesives at different concentrations. (p) Adhesion performance of the PGBAP hydrogel in various rat organs, including heart, liver, spleen, lung and kidney. Data are presented as the mean ± standard deviation, $n = 5$.

tissue had a nearly neutral pH. As the pH was higher than the pKa of chitosan (6.5) [26], the amino groups on the chitosan chains became deprotonated, which facilitated the formation of strong intermolecular hydrogen bonds between amino and hydroxyl groups, as well as between adjacent amino groups, promoting the formation of a crosslinked network and leading to the solidification of chitosan. The chitosan network interpenetrated and entangled with the polymer networks on both adhesive surfaces, forming the topological structure shown on the schematic diagram. As a stitching polymer, chitosan connects the two polymer networks much like a suture, enabling stable interconnection between the hydrogels. This stable integration relies primarily on physical

entanglement between the chitosan chains and the polymer chains. To determine the bonding strength of the hydrogel-based nerve conduit interface, a t-peak test was conducted to quantitatively assess the adhesion of hydrogels containing different concentrations of chitosan solution (Fig. S7 in the ESM). During the peeling process, noticeable deformation and crack formation occurred (Fig. 2(n)). The calculated adhesion energy (equivalent to twice the peak adhesion force per unit width) for each chitosan concentration is illustrated in Fig. 2(o). Among the tested concentrations, the 2% w/v chitosan adhesive had the highest adhesion performance, with an adhesion energy of 193.68 ± 13.41 J/m^2 and a peak force of 213.44 ± 17.91 N/m. When the chitosan concentration is too low, the chitosan chains become more dispersed, resulting in reduced entanglement with the polymer chains in the hydrogel nerve conduit. Conversely, an excessively high chitosan concentration increases the viscosity of the adhesive solution, which hinders its infiltration into the hydrogel nerve conduit and ultimately leads to the formation of a thick adhesive layer that compromises adhesion performance [27]. It demonstrated effective bonding with various materials, maintaining its position even under external mechanical stress (Fig. 2(p), and Figs. S8 and S9 in the ESM). This feature highlights its potential for internal applications, demonstrating that it can remain attached under physical forces.

2.4 Physicochemical characterization

To analyze the molecular interactions within the synthesized hydrogels, Fourier transform infrared (FTIR) spectroscopy was conducted on the PGBA and PGBAP samples (Fig. 3(a)). The broad band at about 3218 cm^{-1} corresponded to the O–H stretching vibration, attributed to PVA and gelatin, and possibly to the N–H stretching vibration from ammonium sulfate. The peak at 1711 cm^{-1} was assigned to the C=O stretching vibration. The peak at 1402 cm^{-1} corresponded to the C–H bending vibration, whereas the peak at 1250 cm^{-1} was attributed to the C–O stretching vibration. The absorption at 1068 cm^{-1} occurred due to the S=O stretching vibration from sulfate groups, and the peak at 610 cm^{-1} corresponded to the SO_4^{2-} bending vibration. Additionally, the signal at 1242 cm^{-1} was associated with the C–O stretching vibration related to ester functional groups. After the incorporation of PEDOT:PSS, noticeable peak shifts and changes in intensity were observed in the FTIR spectra. The O–H stretching vibration band exhibited a blue shift accompanied by an increase in intensity, indicating enhanced hydrogen bonding and crosslinking interactions between PEDOT:PSS, PVA, and gelatin. Additionally, the peak area at about 2940 cm^{-1} increased, which could be attributed to the presence of methyl groups in the PEDOT backbone, leading to an intensified vibrational response in this region. Distinct peaks in the range of 1328–1376 cm^{-1} were associated with the asymmetric stretching vibration of B–O–C bonds, arising from interactions between the side chains of PVA and tetrahydroxyborate ions $[B(OH)_4]^-$ [28]. The absorption bands at 939 and 820 cm^{-1} were attributed to the B–O stretching vibration and the B–O–B bending vibration within the $[B(OH)_4]^-$ structure of borax, respectively [29, 30]. The decrease in the intensity of the S=O stretching vibration at 1085 cm^{-1} suggested that the incorporation of PEDOT:PSS may have led to the formation of a new crosslinked network that restricted the vibrational motion of the sulfate groups. This interpretation is supported by the weak bending vibration peak of SO_4^{2-} observed at 605 cm^{-1}.

The results of the X-ray diffraction (XRD) analysis revealed that the intensities of the diffraction peaks at 16.85°, 20.10°, 22.83°, 29.24°, and 33.80° increased significantly following the incorporation of PEDOT:PSS (Fig. 3(b)), which indicated an increase in the crystallinity of the composite material. In the PVA-gelatin matrix, the conductive polymer chains of PEDOT:PSS acted as structural templates during the gelation and freeze-thaw crosslinking process, guiding the ordered assembly of NH_4^+ and SO_4^{2-} ions and reducing lattice distortion. Additionally, electrostatic interactions and hydrogen bonding between the sulfonate groups ($-SO_3-$) on the PEDOT:PSS surface and the NH_4^+ ions further stabilized the crystalline configuration of ammonium sulfate. The porous, crosslinked network formed through the freeze-thaw cycles was also optimized by the presence of PEDOT:PSS, which not only provided abundant nucleation sites for ammonium sulfate crystallization but also modulated the polarity of the solution and diffusion kinetics. This regulation slowed the crystal growth rate, promoting a more uniform grain size and reducing the defect density, ultimately increasing the crystallinity and intensifying the corresponding XRD peaks. These structural improvements contributed to the mechanical reinforcement of the hydrogel.

The results of the X-ray photoelectron spectroscopy (XPS) analysis (Fig. 3(c) and Fig. S10 in the ESM) revealed that the characteristic binding energy peaks of the PGBAP hydrogel were located at about 190, 284, 399, and 532 eV, corresponding to B 1s, C 1s, N 1s, and O 1s, respectively. The B 1s spectrum was deconvoluted into two distinct peaks at 190.08 and 191.54 eV, which were attributed to the B–C and B–O bonding environments, respectively.

2.5 Construction of a mechanically trained, surface-structured, trimmable foldable nerve conduit

With increasing levels of stretching, the surface of the hydrogel gradually developed a topological morphology (Fig. 3(d)). Based on the excellent mechanical foundation of the hydrogel, we first fixed the applied strain at 10% and investigated the effect of different stretching cycles. Subsequently, the number of stretching cycles was fixed, and different strain levels were examined. Specifically, samples with defined dimensions were subjected to cyclic stretching at a fixed strain of 10% for 0, 200, and 500 cycles. Then, while keeping the number of cycles constant at 500, different strain levels of 0%, 5%, and 10% were applied. During the stretching process, each hydrogel was subjected to cyclic stretching at a constant strain rate of 0.14 s^{-1}. The relaxation time between stretching cycles was set to 1 min. The environmental humidity was maintained at 70% relative humidity during stretching at 0, 200, and 500 cycles. The surface texture was observed by scanning electron microscopy (SEM) and confocal microscopy. In contrast, 0% and 5% strains did not result in surface alignment. A maximum strain of 10% was selected because it was sufficient to induce aligned surface patterns while requiring significantly less time and cost than higher strain levels. After 500 cycles of pre-stretching, SEM and laser confocal microscopy examinations revealed the formation of a fibrous topological structure on the surface (Figs. 3(e) and 3(f)). We selected 500 cycles as the optimal point that achieves a stable and consistent surface topology while striking a deliberate balance between experimental efficacy and practical manufacturing considerations. This choice avoids further, non-essential cycles to conserve both time and economic costs, aligning with our core objective of developing an efficient and low-cost strategy for producing reliable hydrogel nerve conduits. The cross-sectional

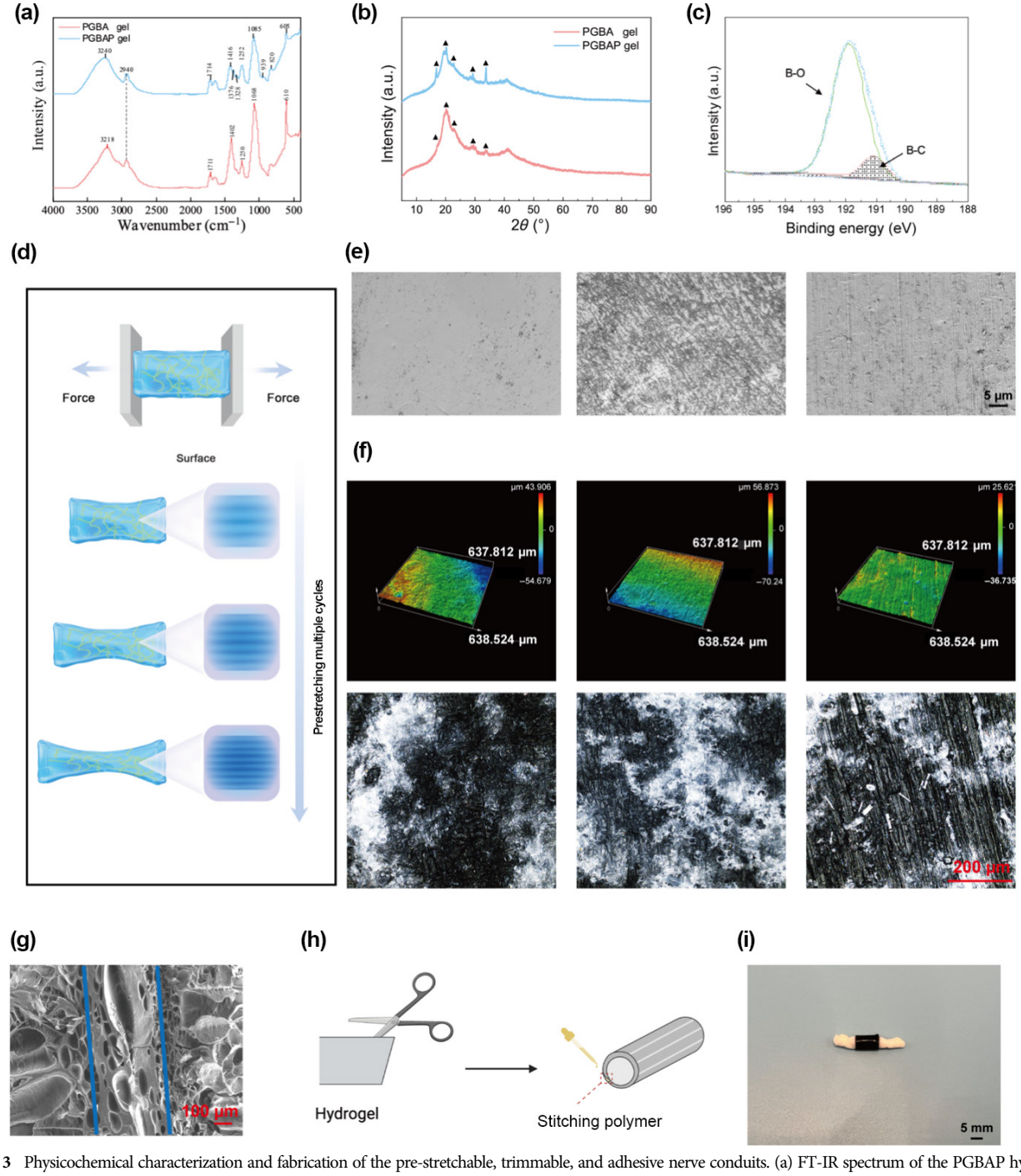

Figure 3 Physicochemical characterization and fabrication of the pre-stretchable, trimmable, and adhesive nerve conduits. (a) FT-IR spectrum of the PGBAP hydrogel. (b) XRD pattern of the PGBAP hydrogel. (c) XPS spectra of the PGBAP hydrogel. (d) Schematic illustration of the pre-stretching strategy applied to the PGBAP hydrogel. Surface morphology of the PGBAP hydrogel under cyclic stretching: (e) SEM images of the hydrogel before pre-stretching (left) and after 200 (middle) and 500 (right) cycles of 10% pre-stretched strain; (f) corresponding 3D (top) and 2D (bottom) confocal microscopy images illustrating the microstructural evolution and surface integrity during repeated mechanical deformation. (g) Cross-sectional SEM image of the PGBAP hydrogel coated with chitosan, showing the interface morphology. (h) Schematic illustration of the origami-inspired PGBAP hydrogel nerve conduit. (i) Macroscopic image of the fabricated PGBAP hydrogel conduit adhered to the porcine sciatic nerve.

morphology of the PGBAP hydrogel adhesive sample after freeze-drying is illustrated in Fig. 3(g). The chitosan adhesive layer appeared smooth and bright, with elliptical pores elongated along the direction parallel to the interface. In contrast, the hydrogel matrix displayed larger pores oriented perpendicular to the interface, especially in regions farther from the interface. It was difficult to clearly distinguish the hydrogel matrix from the chitosan adhesive layer, which indicated that the chitosan solution had penetrated the hydrogel and formed entanglements with the polymer chains. This confirmed the formation of an interfacial adhesion structure between the hydrogel and the chitosan adhesive. The swelling properties of the chitosan-coated PGBAP (PGBAPC), PGBAP, and PGAP hydrogels were characterized. Under the constraint of borate ester bonds within the hydrogel network, PGBAP and PGAP maintained a swelling ratio of about 20% after three days of incubation at 37 °C, which was nearly negligible (Fig.

S11 in the ESM). After cutting and folding, the conduit adhered to the porcine sciatic nerve via the chitosan-based adhesive (Figs. 3(h) and 3(i)), and it remained intact after being soaked in water for 24 h (Video S2 in the ESM). To directly evaluate the risk of mechanical mismatch, we conducted tensile tests to compare the Young's modulus of the PGBAP conduit with that of the native rat sciatic nerve. As shown in Fig. S12 in the ESM, the tensile Young's modulus of the PGBAP nerve conduit was 12.6 ± 1.46 MPa, while that of the rat sciatic nerve was 15.3 ± 3.54 MPa. Statistical analysis revealed no significant difference between the two ($P > 0.05$, Two-Sample t-test). This result indicates that the PGBAP conduit possesses a tensile modulus highly comparable to that of the native nerve tissue, effectively mitigating the risk of mechanical mismatch upon implantation. Such mechanical compatibility is crucial for reducing stress shielding at the implant-tissue interface and facilitating better integration. Additionally, the PGBAP conduit was immersed in phosphate-buffered saline (PBS) and maintained at 37 °C to simulate the modulus loss that may occur when the conduit is exposed to body fluids after implantation. As shown in Figs. S13 and S14 in the ESM, although the compressive modulus of the nerve conduit decreased from an initial 62.15 ± 3.66 kPa to approximately 23.01 ± 7.11 kPa after 4 weeks of immersion, we posit that this mechanical property remains adequate to support sciatic nerve regeneration (Video S3 in the ESM). This claim is supported by two key considerations. First, successful peripheral nerve repair strategies emphasize the importance of mechanical matching between the implant and the native tissue. The modulus of our degraded conduit (~ 23 kPa) falls within the range reported for hydrogels with a "tissue-like" modulus or those explicitly designed to match the mechanical properties of the sciatic nerve [31]. Importantly, studies have shown that hydrogel matrices with stiffness as low as 0.6 kPa can effectively guide neurite outgrowth [32], and advanced hydrogel conduits within the kilopascal range have successfully promoted sciatic nerve regeneration *in vivo* [33]. This indicates that the requirement for mechanical support is not an excessively high absolute value, but rather an appropriate, tissue-compatible range. Second, and more critically, the conduit maintained structural integrity and an open lumen without collapse throughout the immersion period (Video S4 in the ESM), thereby fulfilling the primary mechanical requirement of providing a continuous guidance pathway for regenerating axons. Therefore, the preserved mechanical properties, together with its stable structure, are considered sufficient to provide the necessary support during the critical early phase of nerve repair. After extensive formulation optimization and process refinement, the PGBAP hydrogel prepared under optimal conditions was formed into a nerve conduit.

Based on the continuous optimization of the hydrogel formula in the previous section, the best ratio was obtained, which is 10 wt.% PVA, 10 wt.% gelatin, 0.04 mol/L boric acid, 20 wt.% ammonium sulfates and 10 wt.% PEDOT:PSS. In the subsequent biological experiments, PGBAP was specially prepared with this optimal ratio. The optimized pre-stretched PGBAP gel, obtained under 500 stretching cycles at 10% strain, was referred to as PGBAP-500. The PGBAP-500 hydrogel loaded with NGF was referred to as PGBAP-500-NGF. As a promoting molecule, NGF should be released during the repair process to accelerate regeneration. After loading NGF, pharmacokinetic studies (performed as described in previous studies [34, 35]) showed that the drug release time was as long as 14 days (Fig. S15 in the ESM). The 14-day sustained release of NGF from our hydrogel covers the critical early phase of axonal sprouting and Schwann cell activation, which proved sufficient for functional recovery in the 8 mm defect model studied here. For longer gaps (> 10 mm), extending the release period could be beneficial to maintain continuous trophic support, as the promoting effect of free NGF often diminishes after 1 month due to rapid degradation and clearance [36]. Technologies such as polymeric microspheres (e.g., PLGA-based systems) or mineral-coated microparticles have demonstrated the ability to prolong protein delivery over several weeks and enhance regeneration in longer nerve defects. For instance, poly(phosphoester) microspheres can release bioactive NGF for at least 10 weeks [36], and mineral-coated microparticles have shown sustained release of NGF for at least 22 days *in vitro* and promote myelinated axon growth and functional recovery in a 10 mm graft model [37]. While the current hydrogel matrix provides adequate release for this study, future designs could integrate such sustained-release systems to address more clinically relevant, large-gap injuries.

2.6 Analysis of neuronal differentiation in co-cultured PC12 cells *in vitro*

We used PC12 cells grown on different substrates, including PGBAP, PGBAP-500, and PGBAP-500-NGF, and glass slides as a control to study their responses in an environment that stimulates neural conditions. Because of their high sensitivity to NGF and their ability to develop into neuron-like cells, PC12 cells were central to our analysis [38]. To assess their ability to differentiate into neuron-like structures on these hydrogels, we performed Tuj-1 (β-III tubulin) staining (Fig. 4(a)). Tuj-1 is a marker that specifically targets mature neuronal microtubules and is frequently used to detect the initial stages of neuronal differentiation [11]. PC12 cell differentiation was evaluated based on neurite outgrowth after culture on different substrates (PGBAP, PGBAP-500, PGBAP-500-NGF, and glass control). After three days of co-culture, PC12 cells on PGBAP-500-NGF and PGBAP-500 exhibited pronounced neurite outgrowth and an aligned orientation, indicating that the fibrous topological structure induced by pre-stretching not only promoted the differentiation of PC12 cells but also facilitated the orderly growth of neural cells (Figs. 4(b)–4(d)). Moreover, the PGBAP-500-NGF group presented significant advantages in terms of neurite length and the cell differentiation ratio, indicating that the combination of the pre-stretched structure and NGF loading further promoted neurite outgrowth in PC12 cells. The angular distribution of the cells (Fig. 4(d)) revealed that the PC12 cells in the PGBAP-500 and PGBAP-500-NGF groups exhibited uniformly oriented neurite growth. This alignment along the pre-stretching fibrous direction guides and promotes axonal extension at the site of nerve injury. While the PC12 cell data demonstrates the conduit's ability to support neurite outgrowth and orientation, we acknowledge the inherent limitations of this model. PC12 cells, a rat pheochromocytoma-derived cell line widely used as a neuronal model, cannot replicate the complex functions of primary Schwann cells — the key orchestrators of peripheral nerve regeneration that clear debris, provide trophic support, and ultimately form myelin [39]. Therefore, our *in vitro* results primarily validate the material's biocompatibility, topological guidance, and NGF bioactivity. To address the critical process of myelination beyond PC12 scope, our *in vivo* model serves as the definitive functional test. Histological evidence of remyelination and functional recovery in the rat sciatic

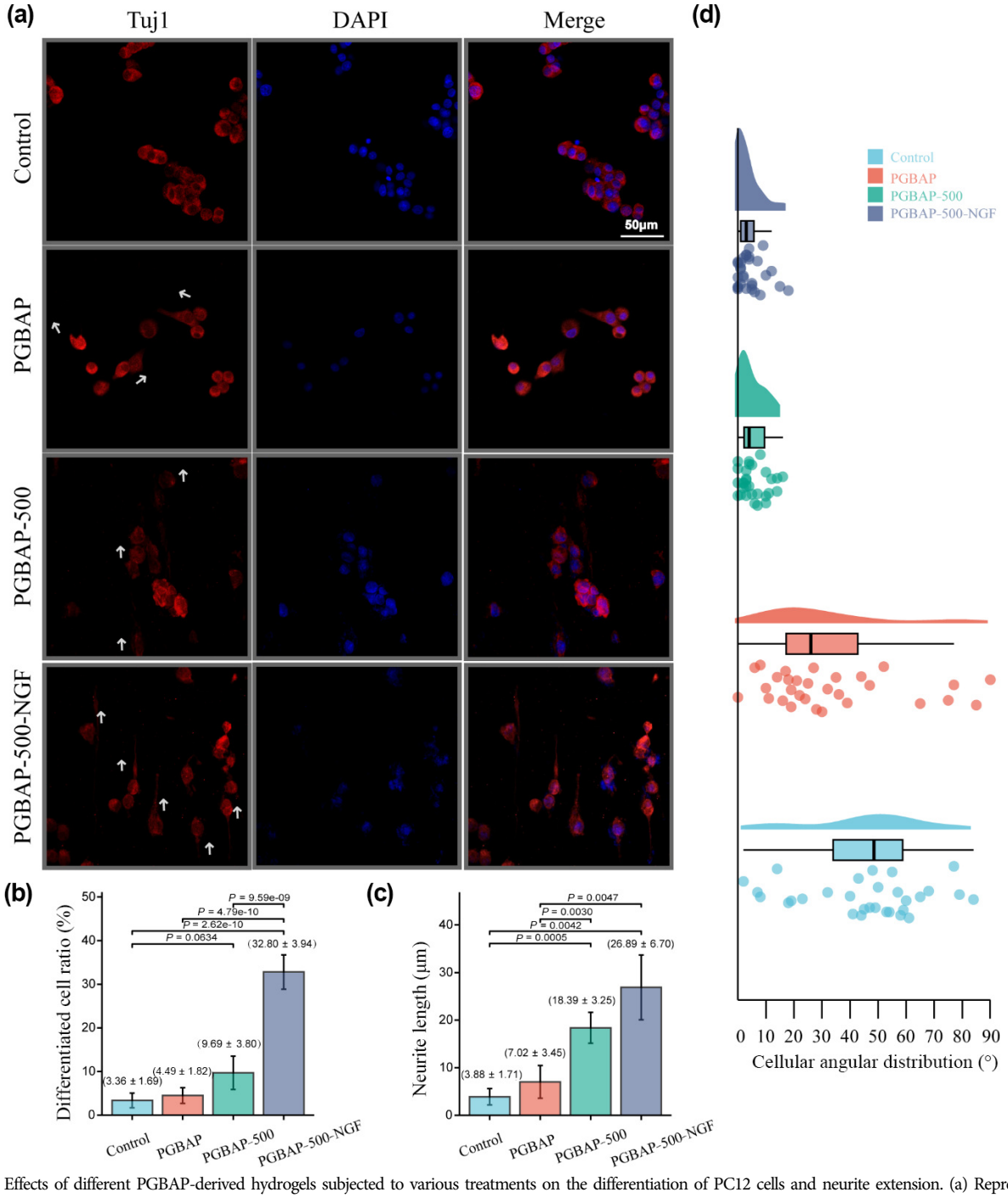

Figure 4 Effects of different PGBAP-derived hydrogels subjected to various treatments on the differentiation of PC12 cells and neurite extension. (a) Representative fluorescence images of PC12 cells cultured on glass slides (control) and PGBAP-derived hydrogels subjected to different treatments (PGBAP, PGBAP-500, and PGBAP-500-NGF) after being cultured in a differentiation medium for three days (red: Tuj1; blue: 4',6-diamidino-2-phenylindole (DAPI)). (b) Percentages of neurons differentiated from PC12 cells. (c) Neurite length of differentiated PC12 cells. (d) Cellular angularity of differentiated PC12 cells. The scale bar is 50 μm. Data are presented as the mean ± standard deviation, $n = 5$.

nerve defect model directly confirms successful nerve repair, compensating for the lack of direct *in vitro* myelination observation. Future studies employing Schwann cell-neuron co-cultures will specifically investigate myelination dynamics.

2.7 *In vivo* biocompatibility assessment

The biodegradability and biocompatibility of PGBAP-500-NGF were assessed through subcutaneous implantation in Sprague-Dawley (SD) rats, followed by an analysis of systemic toxicity. The regeneration rate of the sciatic nerve in rats is about 1 mm per day [40, 41]. The ideal degradation period for a nerve conduit should be adequate to facilitate essential early nerve regeneration phases while avoiding adverse outcomes associated with the prolonged presence of implants. No evidence of inflammatory or necrotic reactions was found in the tissues adjacent to PGBAP-500-NGF (Fig. S16 in the ESM), and it degraded well after four weeks. Histological

evaluations (Fig. S17 in the ESM) revealed no significant morphological changes in the organs examined. It meets the current requirements of NGCs [40]. These observations confirmed the *in vivo* biocompatibility indicated by earlier *in vitro* tests and revealed that PGBAP-500-NGF breaks down without causing detectable toxic effects, highlighting its suitability for clinical application in neural tissue engineering. While PEDOT:PSS is not considered readily biodegradable, its excellent biocompatibility and safe application in biomedical implants are well-supported. For instance, when PEDOT:PSS was applied in the cultivation of rat bone marrow mesenchymal stem cells, the cells exhibited regular morphology and robust proliferation behavior, indicating the favorable biocompatibility of PEDOT:PSS [42]. More directly relevant to long-term implantation, a patterned PEDOT:PSS hydrogel was reported to maintain stable electrochemical performance and show no signs of toxicity after six months in a physiological environment [43]. Furthermore, in a demanding 12-week *in vivo* model for tendon-bone repair, an electroactive suture containing PEDOT effectively promoted healing without eliciting adverse inflammatory responses or systemic toxicity [44]. Regarding clearance, the PSS component may gradually dissolve in physiological fluids, with fragments potentially being metabolized at low release rates [45]. The absence of observed toxicity in our study aligns with these reports, supporting the material's biocompatibility for the critical nerve regeneration period. Further investigation into its precise long-term fate in neural applications remains a valuable future direction.

2.8 The PGBAP-500-NGF hydrogel promotes nerve regeneration

As shown in Fig. 5(a), an 8-mm sciatic nerve defect model was established and divided into four groups: the autograft, PGBAP, PGBAP-500, and PGBAP-500-NGF groups. We also investigated the adhesive behavior of the NGCs at the early stage and found that within the first three days, a thin encapsulating tissue formed around the conduit, firmly anchoring it to both nerve stumps (Fig. S18 in the ESM). This phenomenon further ensured the stable integration of our composite nerve conduit within the defect site. At 12 weeks post-implantation, the regenerated nerves and gastrocnemius muscles were evaluated for their pathophysiological and functional recovery. All three types of nerve conduits were tailored, folded, and coated with chitosan adhesive to form tubular structures that adhered securely to the proximal and distal nerve stumps, effectively bridging the defect (Fig. 5(b)). Hematoxylin and eosin (H&E) staining at 12 weeks post-surgery revealed distinct differences in the morphology of regenerated nerves among groups (Fig. S19 in the ESM). The PGBAP group showed discontinuous and disorganized nerve bundles with extensive fibrotic tissue, indicating incomplete regeneration. The PGBAP-500 group displayed moderate connective tissue deposition, suggesting limited yet ongoing regeneration. Notably, the PGBAP-500-NGF group presented continuous and compact fascicular structures with reduced fibrosis, closely resembling the autograft morphology. Macroscopic observation further confirmed that the PGBAP-500-NGF conduit bridged the nerve defect at the injury site, showing continuous tissue connection (Fig. S20 in the ESM). Longitudinal sections of the central defect area were stained with S-100β (a Schwann cell marker) and NF200 (a neurofilament marker). The PGBAP-500 and PGBAP-500-NGF groups presented significantly enhanced and aligned neurofilament structures, which may be attributed to the topological surface features introduced by the pre-stretching process. The PGBAP-500-NGF group presented significantly greater levels of S-100β-positive and NF200-positive fluorescence staining than the PGBAP and PGBAP-500 groups, which can be attributed to the synergistic effects of the aligned topological structure and NGF loading (Fig. 5(c)). Autologous nerve transplantation is the gold standard for treating peripheral nerve injuries, and the regenerative outcomes of the PGBAP-500-NGF group were comparable to those of the autograft group.

Transmission electron microscopy (TEM) examinations were performed to evaluate the remyelination of regenerated sciatic nerves 12 weeks after surgery (Fig. 6(a)). Quantitative analysis was conducted on the parameters of key nerve fibers, including the diameter of the axons, the myelin sheath thickness, and the g-ratio (the ratio of the inner axonal diameter to the total outer fiber diameter). In the disordered hydrogel PGBAP group, TEM examination of the regenerated nerves in transverse sections revealed that the myelinated fibers were sparse and thin. In contrast, the regenerated nerves in the PGBAP-500-NGF group were surrounded by a dense, well-defined, and electron-dense myelin sheath. Statistical analysis (Fig. 6(b)) revealed that the inner diameter of regenerated nerve fibers in the PGBAP-500-NGF conduit group (3.43 ± 1.48) was significantly greater than that in the PGBAP group (1.95 ± 0.87) and was not significantly different from that in the autograft group (3.87 ± 1.40). The aligned PGBAP-500 conduit group (2.66 ± 1.07) also presented significantly larger nerve fiber diameters than the PGBAP group. The myelin sheath thickness of regenerated myelinated nerves in the PGBAP-500-NGF group was significantly greater than that in the PGBAP-500 and PGBAP groups, with no significant difference from that in the autograft group (Fig. 6(c)). The g-ratio profile of the PGBAP-500-NGF group closely resembled that of the autograft group (Fig. 6(d)). A decreasing trend in g-ratio values was observed, following the sequence: PGBAP (0.78 ± 0.03), PGBAP-500 (0.72 ± 0.04), PGBAP-500-NGF (0.68 ± 0.04), and autograft (0.66 ± 0.05). The g-ratio of healthy, uninjured sciatic nerves lies between 0.55 and 0.68 [46], which is similar to the values found in our experiments. The PGBAP-500-NGF conduits effectively reduced the g-ratio of regenerated nerves to within this physiological range while also significantly increasing the axonal diameter, approaching the value recorded in autograft repairs.

To evaluate the promoting effect of PGBAP-500-NGF on peripheral nerve regeneration, we assessed the nerve conduction ability through electrophysiology, and we evaluated the re-innervation function of the distal gastrocnemius muscle by recording the compound muscle action potentials (CMAPs) amplitudes. The results showed that the peak value of the PGBAP-500-NGF group was significantly higher than that of the PGBAP-500 and PGBAP groups. In addition, the peak value of the PGBAP-500 group was also significantly higher than that of the PGBAP group (Fig. 6(e) and Fig. S21 in the ESM).

2.9 PGBAP-500-NGF promotes gastrocnemius and functional recovery

The gastrocnemius muscle, innervated by branches of the sciatic nerve, was also evaluated to indirectly assess the function of the

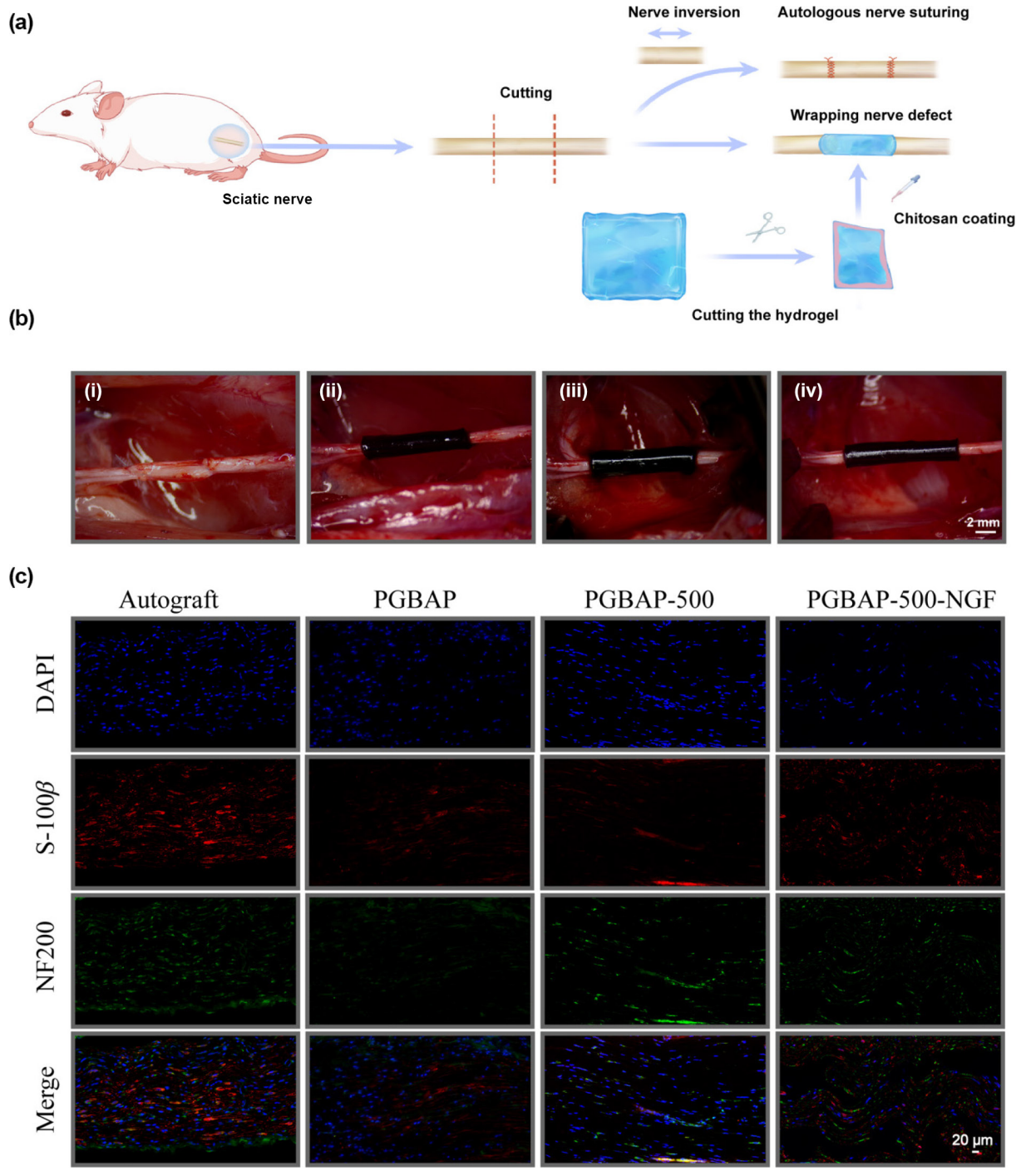

Figure 5 *In vivo* evaluation of the fabricated editable and foldable nerve conduits in an SD rat sciatic nerve defect model. (a) Schematic illustration of the animal model. (b) After an 8 mm defect in the left sciatic nerve of SD rats was created, (i) autologous neurorrhaphy, (ii) PGBAP, (iii) PGBAP-500, and (iv) PGBAP-500-NGF conduits (cut, folded, and adhered to chitosan polymers) were used to bridge the injured gap. (c) Immunofluorescence staining for DAPI (blue), S-100β (red), and NF200 (green) in the corresponding groups three months after surgery.

regenerated nerves. Samples were collected from the injured and uninjured sides of the gastrocnemius muscle (Fig. 7(a)), and the ratio of wet weight between the injured and healthy tissues was calculated. The sciatic functional index (SFI) is a widely applied quantitative parameter for assessing functional impairments associated with sciatic nerve injury. The SFI was calculated through footprint analysis to evaluate *in vivo* functional recovery following PNI (Fig. 7(b)). Gross morphology and Masson's trichrome staining of the gastrocnemius muscle revealed significant atrophy on the injured side in the PGBAP group (Fig. 7(a)). Statistical analysis revealed that the wet weight ratio of the gastrocnemius muscle on the injured side relative to the contralateral side was comparable between the PGBAP-500-NGF group and the autograft group, with no significant difference (Fig. 7(c)). Both groups presented significantly greater muscle mass than the PGBAP and PGBAP-500 conduit groups, with PGBAP-500 being considerably

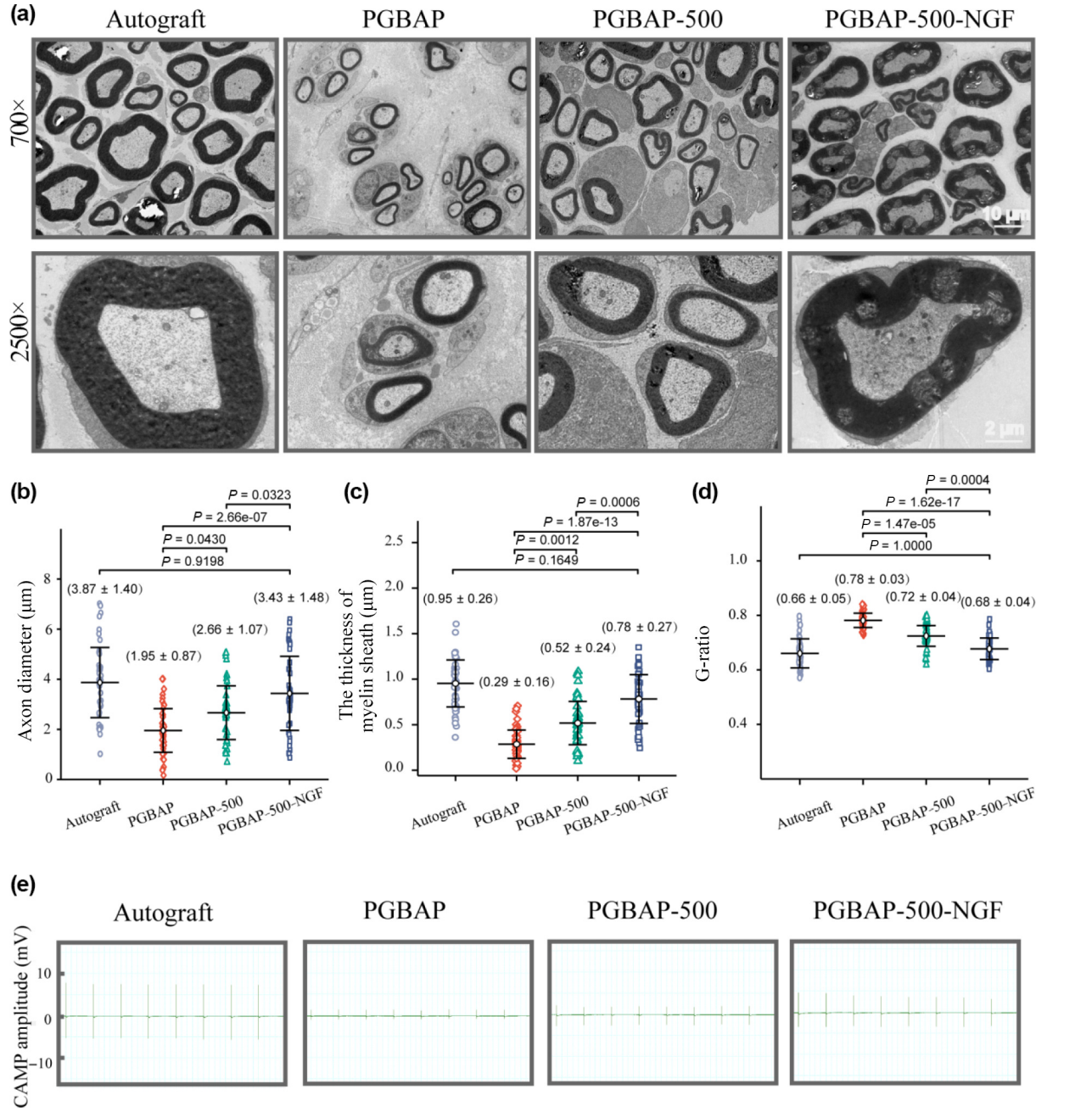

Figure 6 TEM images illustrating the remyelination of regenerated sciatic nerves 12 weeks after surgery. (a) The ultrastructure of myelination. The upper panel presents a low-magnification view, whereas the lower panel presents a high-magnification view. (b) Axon diameter, (c) the thickness of the myelin sheath, (d) g ratio, and (e) representative CMAP recordings from rats in different treatment groups. Data are presented as the mean ± standard deviation, $n = 5$.

greater than PGBAP. Masson staining revealed extensive collagen deposition around the atrophied muscle fibers in the PGBAP group, whereas no tissue fibrosis was found in either the autograft group or the PGBAP-500-NGF group. In the PGBAP-500-NGF group, the muscle fiber area ratio was 70.85% ± 3.78%, which was not significantly different from that in the autograft group (73.38% ± 4.70%) but was significantly greater than that in the PGBAP group (44.49% ± 9.67%). Additionally, the PGBAP-500 group (58.84% ± 7.66%) presented a significantly greater muscle fiber ratio than the PGBAP group (Fig. 7(d)).

The SFI is commonly used to evaluate sciatic nerve function in animal models, especially in rats. This method assesses the degree of nerve injury or recovery by comparing measurements from the injured paw with those from the normal (contralateral) paw [47, 48]. It is calculated using the following parameters: experimental print length (EPL), normal print length (NPL), experimental toe spread (ETS), normal toe spread (NTS), experimental intermediate toe spread (EIT), and normal intermediate toe spread (NIT). The SFI was calculated using the following equation (Eq. (1)):

$$\mathrm{SFI} = -38.8 \times \frac{\mathrm{EPL} - \mathrm{NPL}}{\mathrm{NPL}} + 109.5 \times \frac{\mathrm{ETS} - \mathrm{NTS}}{\mathrm{NTS}} + 13.3 \times \frac{\mathrm{EIT} - \mathrm{NIT}}{\mathrm{NIT}} - 8.8 \quad (1)$$

Generally, SFI values range from about −100, which reflects

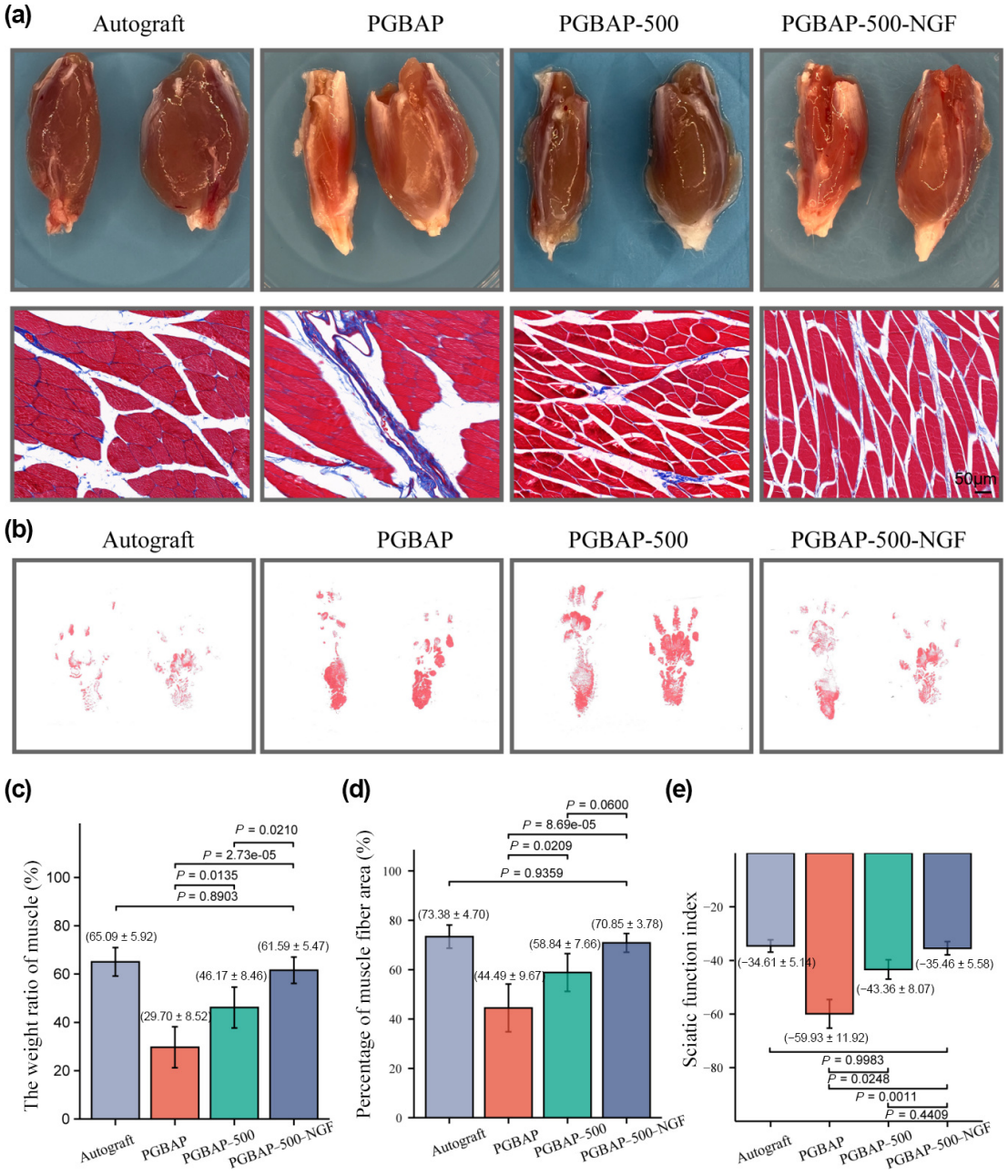

Figure 7 Evaluation of gastrocnemius muscle recovery and functional improvement. (a) Macroscopic view and Masson's trichrome staining of the gastrocnemius muscle 12 weeks after surgery. (b) Footprints of the injured (left) and contralateral (right) sides. (c) Quantitative analysis of the muscle wet weight ratio (injured to contralateral side), (d) percentage of muscle fiber area, and (e) SFI scores for rats in different treatment groups. Data are presented as the mean ± standard deviation, $n = 5$.

significant dysfunction, to 0, which indicates normal or nearly normal recovery of function. Footprints from the PGBAP-500-NGF conduits improved, much like those from the autografts, whereas this type of recovery was not observed in the PGBAP conduits (Fig. 7(b)). The SFI scores were similar between PGBAP-500-NGF and autografts, but both were significantly greater than those in the PGBAP conduit group (Fig. 7(e)).

2.10 PGBAP-500-NGF provided a pro-regenerative microenvironment for nerve regeneration compared with PGBAP

To elucidate the mechanism by which PGBAP-500-NGF promotes peripheral nerve regeneration, we employed RNA sequencing to profile transcriptional alterations across the different treatment groups. A Venn diagram illustrated the overlap and distinction of DEGs among the three groups: PGBAP-500-NGF, PGBAP-500, and PGBAP (Fig. 8(a)). Specifically, the comparison between the PGBAP-500-NGF and PGBAP groups identified 705 upregulated and 309 downregulated genes. Hierarchical clustering analysis based on these DEGs revealed distinct gene expression profiles that clearly segregated the three groups (Fig. 8(b)). Kyoto Encyclopedia of Genes and Genomes (KEGG) pathway enrichment analysis indicated that the DEGs between PGBAP-500-NGF and PGBAP were significantly involved in terms related to tissue repair and regeneration, including the Calcium signaling pathway, AMPK signaling pathway, PPAR signaling pathway, and Adipocytokine signaling pathway (Fig. 8(c)).

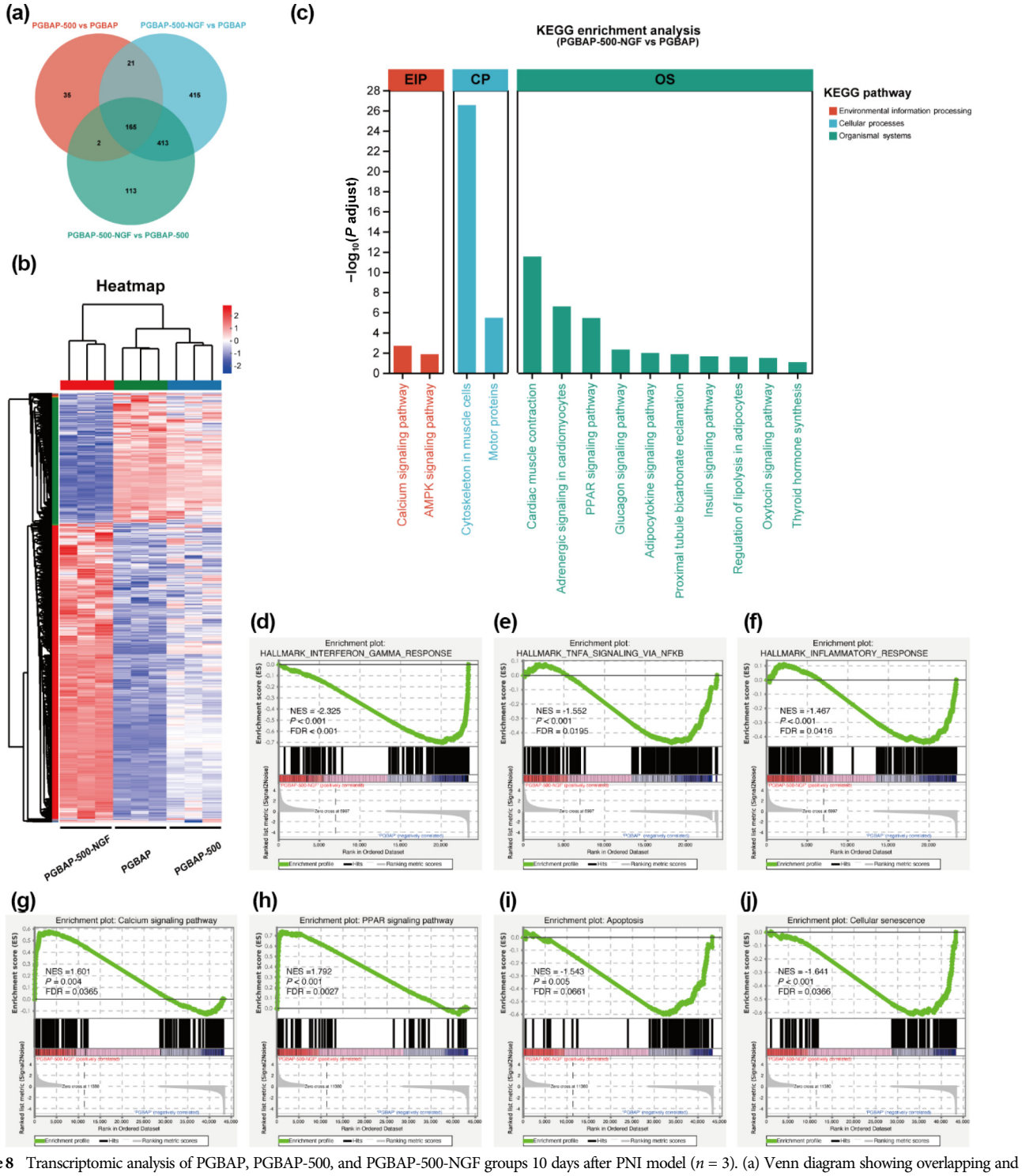

Figure 8 Transcriptomic analysis of PGBAP, PGBAP-500, and PGBAP-500-NGF groups 10 days after PNI model (n = 3). (a) Venn diagram showing overlapping and unique differentially expressed genes among the three groups. (b) Cluster analysis of target genes across the groups. (c) KEGG pathway analysis of differentially expressed genes between PGBAP-500-NGF and PGBAP groups. The horizontal axis represents KEGG pathway names, categorized into environmental information processing (EIP), cellular processes (CP), and organismal systems (OS). (d) GSEA analysis of HALLMARK_INTERFERON_GAMMA_RESPONSE. (e) GSEA analysis of HALLMARK_TNFA_SIGNALING_VIA_NFKB. (f) GSEA analysis of HALLMARK_INFLAMMATORY_RESPONSE. (g) GSEA analysis of calcium signaling pathway. (h) GSEA analysis of PPAR signaling pathway. (i) GSEA analysis of apoptosis-related pathways. (j) GSEA analysis of cellular senescence-related pathways.

Gene Set Enrichment Analysis (GSEA) of the significantly enriched gene sets based on FDR revealed seven pathways associated with nerve regeneration. Of these top GSEA results, 2 activated and 5 inactivated biological processes were identified as activated and suppressed in the PGBAP-500-NGF group, respectively. This designation is based on the sign of the Normalized Enrichment Score (NES). Specifically, a positive NES denotes activation of the biological process, and a negative NES denotes its suppression. Notably, several pro-inflammatory signaling pathways were significantly inhibited in the PGBAP-500-

NGF group, including HALLMARK_INTERFERON_GAMMA_RESPONSE, HALLMARK_TNFA_SIGNALING_VIA_NFKB and HALLMARK_INFLAMMATORY_RESPONSE (Figs. 8(d)–8(f)). An appropriate inflammatory response is crucial for peripheral nerve repair. In contrast, excessive or prolonged inflammation disrupts Schwann cell reprogramming, leading to impaired myelin clearance and delayed axonal regeneration. Such defective Schwann cell responses ultimately contribute to failed nerve regeneration [49]. A subdued inflammatory response fosters a pro-regenerative microenvironment for nerve repair [50]. In addition, GSEA indicated that the calcium signaling pathway and PPAR signaling pathway were upregulated in the PGBAP-500-NGF group, while apoptosis and cellular senescence pathways were downregulated. GSEA analysis revealed that PGBAP-500-NGF upregulated calcium and PPAR signaling while downregulating apoptosis and cellular senescence pathways (Figs. 8(g)–8(j)). Enhanced calcium signaling likely promotes Schwann cell proliferation, migration, and neurotrophic support, facilitating axonal regrowth [51]. Activation of PPAR signaling may reduce inflammation and support Schwann cell repair and remyelination [52]. Mechanistically, PPAR-γ activation promotes axonal growth by inhibiting the downstream Rho/ROCK pathway, which otherwise constrains neuronal regeneration [53]. Concurrently, activation of the AMPK/PGC-1α/PPAR-γ axis can polarize macrophages toward a pro-regenerative M2 phenotype, enhancing the repair microenvironment [54]. Translational clinical evidence further supports this role, demonstrating that treatment with a PPAR-α agonist (fenofibrate) directly stimulated corneal nerve regeneration and improved functional outcomes in patients with diabetic neuropathy [55]. Collectively, these findings underscore the therapeutic potential of modulating the PPAR pathway. Together, these changes create a favorable microenvironment that contributes to improved nerve regeneration.

3 Experimental

3.1 Materials

Gelatin, PVA (alcoholysis degree ~ 99%, average degree of polymerization ~ 1700), borax ($Na_2B_4O_7{\cdot}10H_2O$), and ammonium sulfate were acquired from Aladdin Bio-Chem Technology Co., Ltd. All other reagents were of analytical grade and used without additional purification. Deionized water obtained from the laboratory was used for all hydrogel synthesis procedures. The NGF protein and rat NGF enzyme-linked immunosorbent assay (ELISA) kits were purchased from MedChemExpress (MCE) and Shanghai Jonlnbio Industrial Co., Ltd. The anti-βIII-tubulin polyclonal antibody, S-100β polyclonal antibody, NF200 monoclonal antibody and the corresponding secondary antibody were purchased from Proteintech, Inc. DAPI was purchased from Invitrogen.

3.2 Preparation of hydrogels

Different concentrations of PVA solutions were prepared by dissolving 5, 10, and 15 g of PVA in 85, 80, and 75 mL of deionized water, respectively. The mixtures were stirred at 90 °C for 1 h until homogeneous solutions were obtained. These variations in concentration were designed to determine the effects of the PVA content on the physical properties of the hydrogel. After the PVA solution was cooled to 55 °C, 5, 10, and 15 g of gelatin powder were added to the respective solutions. The PGBAP hydrogel was synthesized by incorporating 10 mL of a PEDOT:PSS dispersion into the system. Each mixture was stirred at 55 °C for 40 min until fully dissolved and uniformly mixed. The resulting solutions were poured into polytetrafluoroethylene (PTFE) molds (12 cm × 6 cm × 2 mm) and incubated at −4 °C for 1 h to facilitate initial gelation. The hydrogels were then subjected to three freeze-thaw cycles (−80 °C for 12 h, 25 °C for 12 h) to promote PVA crystallization and strengthen the network structure. The freezing temperature was set at −80 °C for 6 h, followed by thawing at 25 °C for 2 h under a free-thawing protocol. After the freeze-thaw cycles, the samples were immersed in ammonium sulfate solutions (10%, 15%, 20%, and 30%, w/v) containing borax at concentrations of 0.01, 0.04, and 0.08 mol/L for 8 h. The treated hydrogels were then stored for further use. It should be noted that when using the hydrogel, the surface of the hydrogel needs to be carefully rinsed with deionized water for several times to remove the remaining salt ions in the gel. To fabricate the nerve conduits, the pre-stretching strains were carefully optimized to achieve desirable structural properties. The PGBAP hydrogel conduits were stretched using a universal testing machine (Instron 5943, Instron, USA). Following pre-stretching, the hydrogel samples were folded into nerve conduits using an origami-inspired method. Before use, the hydrogels were sterilized via ultraviolet (UV) light. To load NGF, the PGBAP-500 hydrogels were immersed in a 5 μg/mL NGF/PBS solution at 4 °C for 8 h.

3.3 NGF loading and *in vitro* release kinetics

To load NGF, PGBAP-500 hydrogels were immersed in a 5 μg/mL NGF/PBS solution and incubated at 4 °C for 8 h. After loading, the hydrogels were gently rinsed with PBS thrice (5 min each) to remove loosely adsorbed NGF from the surface. The total amount of NGF loaded per conduit (M0) was determined indirectly by quantifying the NGF concentration remaining in the residual loading solution and the washing PBS using an NGF ELISA kit, following the manufacturer's instructions. For the NGF release study, NGF-loaded hydrogels were incubated in a defined volume of PBS at 37 °C under gentle shaking. At predetermined time points (days 1, 3, 5, 7, 9, 11, and 13), the hydrogels were transferred into fresh PBS to maintain sink conditions, and the collected release medium was analyzed by ELISA. The cumulative amount of NGF released at the i^{th} time point ($M_{\text{cumulative},n}$) was calculated as follows (Eq. (2)).

$$M_{\text{cumulative},n} = \sum_{i=1}^{n} (C_i \times V_s) \tag{2}$$

where C_i is the NGF concentration measured at the i^{th} time point and V_s is the volume of the collected release medium. The cumulative NGF release was expressed as a percentage of the total loaded NGF according to Eq. (3).

$$\text{Cumulative release}\ (\%) = \frac{M_{\text{cumulative},n}}{M_0} \times 100\% \tag{3}$$

3.4 Preparation of chitosan adhesives

A 0.2 M 2-(*N*-morpholino) ethanesulfonic acid (MES) buffer solution was diluted with deionized water to a final concentration of 0.1 M. Then, 0.6 g of chitosan powder was dissolved in 30 mL of 0.1 M MES buffer using a magnetic stirrer to obtain a 2% w/v chitosan adhesive. Similarly, 1% w/v and 3% w/v chitosan adhesives were prepared by dissolving the appropriate amounts of chitosan in

10 mL of 0.1 M MES buffer for each concentration and then stored at 4 °C for later use.

3.5 Mechanical test

The mechanical properties of the hydrogels, including their uniaxial tensile and cyclic tensile behavior, were evaluated using a universal testing machine. The hydrogels were prepared according to the JIS-K6215-7 standard dimensions (1 mm thickness × 2 mm width × 12 mm gauge length) [56]. To conduct the uniaxial tensile tests, the initial distance (L0) between the two clamps was set to 12 mm, and the samples were stretched upward at a strain rate of 0.14 s^{-1} until failure. In the cyclic tensile tests, the PGBAP hydrogels were stretched upward to a maximum strain of 1 mm/mm at the same strain rate (0.14 s^{-1}) and then released back to the initial strain at the same rate. For the compression tests, samples with dimensions of 12 mm × 4 mm were compressed at a rate of 4 mm/min. The test was stopped when the strain reached 60%, and the stress corresponding to this strain was recorded as the compressive strength. All tests were conducted at room temperature (22 °C), and the results represent the average of three independent measurements. Conductivity was measured by directly inserting probes into disc-shaped hydrogels with a diameter of 10 mm and a thickness of 1 mm. A 4-point probe resistivity measurement system (RTS-9) was used to determine the conductivity. Measurements were recorded at six different points on each hydrogel to obtain an average value.

3.6 Physicochemical characterization

The dried hydrogels were ground into a powder and fixed with conductive adhesive for XPS analysis using an AXIS SUPRA+ spectrometer (Japan) with argon (Ar) as the ion source. The chemical structure of the hydrogels was characterized by FTIR (SOE-065, Thermo Fisher Scientific, USA) within the wavenumber range of 4000–500 cm^{-1}. XRD analysis was conducted on vacuum-dried hydrogel samples using a Bruker-AXS D8 diffractometer (Germany) to determine their composition and crystallinity, with a copper (Cu) target and a scanning speed of 5 °/min.

3.7 Microstructural observation of hydrogels

The microstructure of the hydrogels was examined by SEM (GEMINISEM 500, Zeiss, Germany). Pre-stretched hydrogel samples were cut into dimensions of 0.5 cm (length) × 0.2 cm (width) × 0.1 cm (thickness) and then immersed in liquid nitrogen for 2 min for supercritical drying to remove moisture. The dried samples were immediately transferred to a freeze dryer until they were completely dehydrated, followed by gold sputter coating before imaging. SEM examinations were conducted at an accelerating voltage of 12 kV, which could be adjusted based on image clarity. The surface morphology was examined using a laser scanning confocal microscope (LEXT OLS5100, Olympus, Japan). Hydrogel samples with dimensions of 3 cm (length) × 1.5 cm (width) × 0.1 cm (thickness) were placed at the center of the microscope stage. Side lighting and adjustable magnification were used to visualize the morphology of the surface of hydrogels.

3.8 Neuronal cell differentiation and regulation *in vitro*

The PC12 cells were obtained from the Shanghai Cell Bank of the Chinese Academy of Sciences. These cells were cultured in RPMI 1640 medium supplemented with 5% fetal bovine serum (FBS), 10% horse serum (HS), and Penicillin/Streptomycin, and maintained in an incubator at 37 °C with an atmosphere of 95% air and 5% CO_2. PC12 cells were cultured on glass slides (control group), PGBAP hydrogels, PGBAP-500 hydrogels, or PGBAP-500-NGF hydrogels. For experiments aimed at inducing differentiation, the culture medium was adjusted to contain 1% HS and 0.5% FBS, and this formulation was maintained for three days. Then, the cells were incubated for 10 min at room temperature in 4% paraformaldehyde solution. The samples were washed three times with cold PBS. The samples were incubated for 10 min in 0.1% Triton X-100 in PBS and then rinsed three times. The cells were treated with 1% bovine serum albumin (BSA) and 0.1% Tween 20 in PBS for 30 min. The samples were incubated overnight with anti-βIII-tubulin antibodies (1:200 dilution) in PBST with 1% BSA at 4 °C. The samples were washed three times with PBS and then incubated with secondary antibodies at room temperature for 1 h in the dark. After DAPI staining, the cells were observed, and images were captured under a confocal microscope. Cells were defined as differentiated cells when they exhibited at least one neurite with a length equal to or greater than the diameter of the cell body, a criterion commonly used to assess neuronal differentiation [57]. Neurite length was quantified from Tuj-1 immunofluorescence images using ImageJ software (National Institutes of Health (NIH), USA). For each differentiated cell, the longest neurite was measured and used for statistical analysis. The differentiation ratio was calculated as the percentage of differentiated cells relative to the total number of cells in each field of view. Neurite orientation was determined by measuring the angle between the principal axis of the neurite and the pre-stretching direction of the hydrogel fibers. Angular measurements were performed using ImageJ, and the angular distribution of neurite growth was plotted to evaluate the degree of alignment. A narrower angular distribution indicated a higher degree of directional neurite growth along the fibrous topology.

3.9 Animal experiment

3.9.1 Animal models

The study protocols were approved by the ethics committee of China Medical University. All procedures involving animals were performed in strict adherence to the guidelines of the China Medical University Animal Care and Use Committee and received approval from the Institutional Review Board (Ethical code: 2024PS1373K). Adult Sprague-Dawley rats (200–250 g) were divided into four groups: autografts, PGBAP, PGBAP-500, and PGBAP-500-NGF implants (n = 5 per group). The animals were anesthetized with isoflurane inhalation and placed in the prone position. A 2 cm incision was made along the femoral axis to expose the sciatic nerve by separating the thigh muscles. An 8 mm segment of the sciatic nerve was excised to create a defect, which, in the autograft group, was reversed and anastomosed using 9–0 sutures. For the biomimetic hydrogel group, PGBAP, PGBAP-500, and PGBAP-500-NGF were cut into 10 mm long rectangles and manually curled. For the hydrogel NGCs groups, the two ends of the nerve were simply connected with 9–0 absorbable sutures, with a length retained in the middle equal to the defect length (8 mm) to increase stability. Then, the edges were coated with chitosan adhesive polymers. The fabricated NGCs were subsequently implanted to bridge the proximal and distal ends of the nerve defects. Three months after surgery, assessments of sciatic nerve regeneration, and morphological and functional evaluations of the gastrocnemius muscle were conducted. Besides, nine rats were

evenly divided into three groups: PGBAP, PGBAP-500, and PGBAP-500-NGF (n = 3 per group). Tissue samples were collected ten days after surgery for transcriptomic analysis.

For *in vivo* biodegradation and biocompatibility test, a PGBAP-500-NGF disc with a diameter of 1 cm and thickness of 1 mm was subcutaneously implanted on the back of an SD rat. Tissue samples were collected at one, two-, and four-weeks post-implantation (n = 3 per group). The hearts, livers, spleens, lungs, and kidneys of the rats in both the implanted and non-implanted PGBAP-500-NGF groups were collected and processed for H&E staining.

3.9.2 Regenerated nerve and gastrocnemius muscle evaluation

At 12 weeks after the operation, footprints, electromyogram signals, regenerated nerves and gastrocnemius muscles were collected for further testing. The collected nerves and gastrocnemius muscles were fixed with 4% paraformaldehyde (PFA), followed by dehydration and paraffin embedding. Gastrocnemius muscle sections were stained using the Masson Kit. Regenerative nerve sections were immunofluorescence stained with anti-S-100 antibody (1:200 dilution) and anti-NF200 antibody (1:200 dilution). For further analysis of the regenerated myelin sheath at the defect site, the regenerated nerve after the operation was immersed in electron microscopy fixative and then embedded in epoxy resin. Ultrathin sections of the samples were performed using uranyl acetate and lead citrate, then, the electron microscope images were taken using the Hitachi H-600 TEM system. At 12 weeks after the operation, the postoperative functional recovery was evaluated by the Powerlab physiological recorder (PowerLab PL3508, ADInstruments, Australia), with the method referring to the previous operation. After anesthetizing the rats, the postoperative sciatic nerve was re-exposed. Bipolar electrodes are connected to the proximal end of the regenerated nerve for stimulation to generate electrical signals. The stimulation is applied in the form of pulses, and another electrode was inserted into the ipsilateral gastrocnemius muscle to record CMAP. The image analysis was conducted using ImageJ.

3.9.3 Transcriptome sequencing and analysis

Total RNA was isolated from regenerated nerve tissues using TRIzol® Reagent. RNA purity and integrity were determined using a 5300 Bioanalyzer (Agilent), and RNA concentration was quantified with an ND-2000 spectrophotometer (NanoDrop Technologies). Transcriptome sequencing was carried out by ShanghaiMajorbio Bio-pharm Biotechnology Co., Ltd. (Shanghai, China). Raw paired-end reads underwent quality filtering and adapter removal with fastp (default parameters) [58]. The high-confidence clean reads were then aligned to the designated reference genome (Rattus norvegicus, version GRCr8) using HISAT2 [59] with the strand-specific alignment option enabled. Finally, a reference-based assembly of the mapped reads from each sample was performed by StringTie [60] to reconstruct the transcriptome of each sample.

Differential expression analysis was performed across the three experimental groups (PGBAP-500-NGF, PGBAP-500, and PGBAP) by conducting all possible pairwise comparisons. Gene expression was quantified using RSEM [61] with transcripts per million (TPM) values, and the statistical significance of differences was assessed using the DESeq2 [62] package. Genes were defined as significantly differentially expressed (DEGs) if they met the thresholds of $|\log_2(\text{fold change})| \geq 1$ and a false discovery rate (FDR)-adjusted P-value < 0.05 in any of the pairwise comparisons.

For downstream functional investigation, the specific set of DEGs identified from the comparison between the PGBAP-500-NGF and PGBAP groups was selected. This gene set was used to perform hierarchical clustering of all samples, revealing global expression patterns. Additionally, KEGG pathway enrichment analysis was conducted on these DEGs to identify significantly perturbed biological pathways, using a Benjamini-Hochberg corrected P-value (P adjust) < 0.05 as the significance cutoff. These analyses were performed on the Majorbio Cloud Platform (https://cloud.majorbio.com/) [62].

For GSEA, the pre-defined "Hallmark Gene Sets" from the Molecular Signatures Database (MSigDB, V7.2) [63] and gene sets from KEGG database were used and converted to rat homologs for re-mapping. The input gene list was generated by ranking all genes according to their Signal2Noise ratio, which reflects the magnitude of expression differences between the PGBAP-500-NGF and PGBAP groups. A Benjamini-Hochberg corrected P-value (P adjust) threshold of < 0.25 was applied to define statistically significant enrichment.

3.10 Statistical analysis

All experiments were independently repeated at least three times to ensure data reliability. Quantitative results are presented as mean ± standard deviation. Differences between two groups were analyzed using an unpaired Student's t-test, while comparisons among three or more groups were performed using one-way analysis of variance (ANOVA), unless otherwise specified. All statistical analyses were conducted using R software (version 4.2.1). A P value less than 0.05 was considered to indicate statistical significance.

4 Conclusions

To summarize, inspired by the cut-and-fold technique, we fabricated customizable conduits for nerve regeneration while applying mechanical cyclic training to impart a fibrous-like surface topology to the material. The evaluation of the nerve conduit mainly comprises three stages: the optimization of the hydrogel system and characterization of its mechanical properties, the formation of a fibrous surface topology under mechanical training, and the fabrication of the conduit for *in vivo* transplantation and functional validation. The main materials consisted of PVA and gelatin. Through freezing and thawing, salting out, incorporation of borate ester bonds and PEDOT:PSS, and continuous optimization of their ratios, a PVA/gelatin/boric acid/ammonium sulfate/PEDOT:PSS system was developed. This system resulted in a stable hydrogel under physiological conditions, excellent energy dissipation, fatigue resistance, stretchability, swelling resistance, and enhanced conductivity. It can be used in combination with NGF and other therapeutic agents. After repeated mechanical training under pre-stretching, a stable fibrous surface topology was formed after 500 cycles of stretching at 10%. When co-cultured with PC12 cells, this topology facilitated their orderly and parallel growth. Finally, by taking advantage of the strong adhesive properties of chitosan-modified polymers, the hydrogel was cut, rolled, and secured to the injured ends of the rat sciatic nerve. The pre-stretched fibrous surface, combined with NGF loading, synergistically promoted the orderly growth of regenerating nerves and markedly enhanced functional recovery. During the early stage of nerve regeneration, it also modulated the microenvironment by suppressing inflammation, activating the calcium signaling and PPAR pathways, and reducing cellular senescence and apoptosis,

thereby establishing a niche conducive to nerve repair and regeneration. This study demonstrated that the newly prepared conduit for nerve repair, featuring surface topology, customizability, and excellent mechanical properties, is highly promising for clinical translation.

Electronic Supplementary Material: Supplementary material (design strategy, electrical conductivity, hydrogel mechanical properties, XPS spectrum, swelling ratio, drug release profiles, macroscopic and histological images of regenerating sciatic nerves, and quantification of CMAP amplitudes) is available in the online version of this article at https://doi.org/10.26599/NR.2026.94908570.

Data availability

All data needed to support the conclusions in the paper are presented in the manuscript and the Electronic Supplementary Material. Additional data related to this paper may be requested from the corresponding author upon request.

Acknowledgements

This work is granted by the Sichuan Science and Technology Program (No. 2024NSFSC1015), Liaoning Province Joint Science and Technology Project (No. 2023JH2/101700164), the China Postdoctoral Science Foundation (No. 2025M772042), the National Natural Science Foundation of China (No. 52272278), the State Key Laboratory of New Ceramic Materials Tsinghua University (No. KF202529), and the China Scholarship Council (No. 202506210326).

Authorship contribution statement

X. Y. H.: Conceptualization, data curation, writing – original draft preparation. Z. C.: Software, validation. E. C. Z.: Visualization, investigation, writing – reviewing and editing. Y. K. M.: Visualization, resources, formal analysis. Z. W. F.: Writing – reviewing and editing. X. D. S.: Supervision, methodology. C. L. L.: Supervision, conceptualization, software. A. H. W.: Supervision, conceptualization, methodology.

Declaration of competing interest

The authors declare that they have no known competing financial interests or personal relationships that could have appeared to influence the work reported in this paper.

Informed consent

Not applicable.

Ethics statement

The animal experiments were carried out following the guidelines of the China Medical University Animal Care and Use Committee and were approved by the Institutional Review Board (Ethical code: 2024PS1373K).

Use of AI statement

None.

References

[1] Ciaramitaro, P.; Mondelli, M.; Logullo, F.; Grimaldi, S.; Battiston, B.; Sard, A.; Scarinzi, C.; Migliaretti, G.; Faccani, G.; Cocito, D. et al. Traumatic peripheral nerve injuries: Epidemiological findings, neuropathic pain and quality of life in 158 patients. *J. Peripher. Nerv. Syst.* **2010**, *15*, 120–127.

[2] Vijayavenkataraman, S. Nerve guide conduits for peripheral nerve injury repair: A review on design, materials and fabrication methods. *Acta Biomater.* **2020**, *106*, 54–69.

[3] Kuffler, D. P. PRP and other techniques for restoring function across peripheral nerve gaps. *J. Neurorestoratol.* **2024**, *12*, 100131.

[4] Nichols, C. M.; Brenner, M. J.; Fox, I. K.; Tung, T. H.; Hunter, D. A.; Rickman, S. R.; Mackinnon, S. E. Effects of motor versus sensory nerve grafts on peripheral nerve regeneration. *Exp. Neurol.* **2004**, *190*, 347–355.

[5] Mokarram, N.; Dymanus, K.; Srinivasan, A.; Lyon, J. G.; Tipton, J.; Chu, J.; English, A. W.; Bellamkonda, R. V. Immunoengineering nerve repair. *Proc. Natl. Acad. Sci. USA* **2017**, *114*, E5077–E5084.

[6] Grinsell, D.; Keating, C. P. Peripheral nerve reconstruction after injury: A review of clinical and experimental therapies. *Biomed. Res. Int.* **2014**, *2014*, 698256.

[7] Leal-Egaña, A.; Díaz-Cuenca, A.; Boccaccini, A. R. Tuning of cell-biomaterial anchorage for tissue regeneration. *Adv. Mater.* **2013**, *25*, 4049–4057.

[8] Zhang, D. T.; Li, Z. M.; Shi, H. F.; Yao, Y. J.; Du, W.; Lu, P.; Liang, K. J.; Hong, L. J.; Gao, C. Y. Micropatterns and peptide gradient on the inner surface of a guidance conduit synergistically promotes nerve regeneration *in vivo*. *Bioact. Mater.* **2022**, *9*, 134–146.

[9] Rutkowski, G. E.; Miller, C. A.; Jeftinija, S.; Mallapragada, S. K. Synergistic effects of micropatterned biodegradable conduits and Schwann cells on sciatic nerve regeneration. *J. Neural Eng.* **2004**, *1*, 151–157.

[10] Yan, Y. X.; Yao, R. T.; Zhao, J. Y.; Chen, K. L.; Duan, L. R.; Wang, T.; Zhang, S. J.; Guan, J. P.; Zheng, Z. Z.; Wang, X. Q. et al. Implantable nerve guidance conduits: Material combinations, multi-functional strategies and advanced engineering innovations. *Bioact. Mater.* **2022**, *11*, 57–76.

[11] Xu, D. Y.; Fu, S. Q.; Zhang, H.; Lu, W. C.; Xie, J. D.; Li, J. L.; Wang, H.; Zhao, Y. J.; Chai, R. J. Ultrasound-responsive aligned piezoelectric nanofibers derived hydrogel conduits for peripheral nerve regeneration. *Adv. Mater.* **2024**, *36*, 2307896.

[12] Lin, S. T.; Liu, J.; Liu, X. Y.; Zhao, X. H. Muscle-like fatigue-resistant hydrogels by mechanical training. *Proc. Natl. Acad. Sci. USA* **2019**, *116*, 10244–10249.

[13] Sun, X.; Mao, Y. M.; Yu, Z. Y.; Yang, P.; Jiang, F. A biomimetic "salting out-alignment-locking" tactic to design strong and tough hydrogel. *Adv. Mater.* **2024**, *36*, 2400084.

[14] Zhang, H.; Xu, D. Y.; Zhang, B.; Li, X. F.; Li, M. L.; Zhang, C.; Wang, H.; Zhao, Y. J.; Chai, R. J. PEDOT-integrated fish swim bladders as conductive nerve conduits. *Adv. Sci.* **2024**, *11*, 2400827.

[15] Feng, Y. H.; Shan, L. J.; Wang, Y. F.; Chen, X. M.; Wang, C.; Liu, J. Conductive hydrogels with topographical geometry and mechanical robustness for enhanced peripheral nerve regeneration. *ACS Nano* **2025**, *19*, 16675–16684.

[16] He, Q. Y.; Huang, Y.; Wang, S. Y. Hofmeister effect - assisted one step fabrication of ductile and strong gelatin hydrogels. *Adv. Funct. Mater.* **2018**, *28*, 1705069.

[17] Chen, W. P.; Hao, D. Z.; Hao, W. J.; Guo, X. L.; Jiang, L. Hydrogel with ultrafast self-healing property both in air and underwater. *ACS Appl. Mater. Interfaces* **2018**, *10*, 1258–1265.

[18] Chen, M. T.; Wu, Y.; Chen, B. H.; Tucker, A. M.; Jagota, A.; Yang, S. Fast, strong, and reversible adhesives with dynamic covalent bonds for potential use in wound dressing. *Proc. Natl. Acad. Sci. USA* **2022**, *119*, e2203074119.

[19] Huang, Z.; Powell, R.; Phillips, J. B.; Haastert-Talini, K. Perspective

on Schwann cells derived from induced pluripotent stem cells in peripheral nerve tissue engineering. *Cells* **2020**, *9*, 2497.

[20] Fang, Y. C.; Wang, C. J.; Liu, Z. B.; Ko, J.; Chen, L.; Zhang, T.; Xiong, Z.; Zhang, L.; Sun, W. 3D printed conductive multiscale nerve guidance conduit with hierarchical fibers for peripheral nerve regeneration. *Adv. Sci.* **2023**, *10*, 2205744.

[21] Liu, C. L.; Jiang, L.; Yue, O. Y.; Feng, Y. F.; Zeng, B. X.; Wu, Y. X.; Wang, Y. F.; Wang, J. Y.; Zhao, L. Y.; Wang, X. M. et al. Thermal enhancement of gelatin hydrogels for a multimodal sensor and self-powered triboelectric nanogenerator at low temperatures. *Adv. Compos. Hybrid Mater.* **2023**, *6*, 112.

[22] Wang, S. T.; Lu, H. T.; Kang, X. C.; Wang, Z. Q.; Yan, S. T.; Zhang, X. H.; Shi, X. T. Electroconductive and immunomodulatory natural polymer-based hydrogel bandages designed for peripheral nerve regeneration. *Adv. Funct. Mater.* **2024**, *34*, 2310903.

[23] Ahmed, S.; Nakajima, T.; Kurokawa, T.; Anamul Haque, M.; Gong, J. P. Brittle-ductile transition of double network hydrogels: Mechanical balance of two networks as the key factor. *Polymer* **2014**, *55*, 914–923.

[24] Kim, J.; Park, J.; Choe, G.; Jeong, S. I.; Kim, H. S.; Lee, J. Y. A gelatin/alginate double network hydrogel nerve guidance conduit fabricated by a chemical-free gamma radiation for peripheral nerve regeneration. *Adv. Healthc. Mater.* **2024**, *13*, 2400142.

[25] Yang, J. W.; Steck, J.; Bai, R. B.; Suo, Z. G. Topological adhesion II. *Stretchable adhesion. Extreme Mech. Lett.* **2020**, *40*, 100891.

[26] Yang, J. W.; Bai, R. B.; Suo, Z. G. Topological adhesion of wet materials. *Adv. Mater.* **2018**, *30*, 1800671.

[27] Cintron-Cruz, J. A.; Freedman, B. R.; Lee, M.; Johnson, C.; Ijaz, H.; Mooney, D. J. Rapid ultratough topological tissue adhesives. *Adv. Mater.* **2022**, *34*, 2205567.

[28] Jiang, M. J.; Zhu, J. D.; Chen, C.; Lu, Y.; Pampal, E. S.; Luo, L.; Zhu, P.; Zhang, X. W. Superior high-voltage aqueous carbon/carbon supercapacitors operating with *in situ* electrodeposited polyvinyl alcohol borate gel polymer electrolytes. *J. Mater. Chem. A* **2016**, *4*, 16588–16596.

[29] Han, J. Q.; Yue, Y. Y.; Wu, Q. L.; Huang, C. B.; Pan, H.; Zhan, X. X.; Mei, C. T.; Xu, X. W. Effects of nanocellulose on the structure and properties of poly(vinyl alcohol)-borax hybrid foams. *Cellulose* **2017**, *24*, 4433–4448.

[30] Qin, Y.; Wang, J. P.; Qiu, C.; Xu, X. M.; Jin, Z. Y. A dual cross-linked strategy to construct moldable hydrogels with high stretchability, good self-recovery, and self-healing capability. *J. Agric. Food Chem.* **2019**, *67*, 3966–3980.

[31] Lee, J.; Choi, Y.; Song, J.; Seong, D.; Jin, S. B.; Ju, J.; Son, D.; Shin, M. Nerve-mimetic adhesive hydrogel electroceuticals: Tailoring *in situ* physically entangled domains in singular polymers. *ACS Nano* **2024**, *18*, 34949–34961.

[32] Liu, H.; Puiggalí-Jou, A.; Chansoria, P.; Janiak, J.; Zenobi-Wong, M. Filamented hydrogels as tunable conduits for guiding neurite outgrowth. *Mater. Today Bio* **2025**, *31*, 101471.

[33] Yu, L.; Bennett, C. J.; Lin, C. H.; Yan, S.; Yang, J. Scaffold design considerations for peripheral nerve regeneration. *J Neural Eng* **2024**, *21*, 041001

[34] Lu, Q. Q.; Li, M. M.; Zou, Y.; Cao, T. Delivery of basic fibroblast growth factors from heparinized decellularized adipose tissue stimulates potent *de novo* adipogenesis. *J. Control. Release* **2014**, *174*, 43–50.

[35] Zhang, S. P.; Lu, Q. Q.; Cao, T.; Toh, W. S. Adipose tissue and extracellular matrix development by injectable decellularized adipose matrix loaded with basic fibroblast growth factor. *Plast. Reconstr. Surg.* **2016**, *137*, 1171–1180.

[36] Xu, X. Y.; Yee, W. C.; Hwang, P. Y. K.; Yu, H.; Wan, A. C. A.; Gao, S. J.; Boon, K. L.; Mao, H. Q.; Leong, K. W.; Wang, S. Peripheral nerve regeneration with sustained release of poly(phosphoester) microencapsulated nerve growth factor within nerve guide conduits. *Biomaterials* **2003**, *24*, 2405–2412.

[37] Hellenbrand, D. J.; Haldeman, C. L.; Lee, J. S.; Gableman, A. G.; Dai, E. K.; Ortmann, S. D.; Gotchy, J. C.; Miller, K. K.; Doucas, A. M.; Nowak, N. C. et al. Functional recovery after peripheral nerve injury via sustained growth factor delivery from mineral-coated microparticles. *Neural Regen. Res.* **2021**, *16*, 871–877.

[38] Li, X. L.; Gluth, A.; Zhang, T.; Qian, W. J. Thiol redox proteomics: Characterization of thiol-based post-translational modifications. *Proteomics* **2023**, *23*, 2200194.

[39] Oprea, D.; Sanz, C. G.; Barsan, M. M.; Enache, T. A. PC-12 cell line as a neuronal cell model for biosensing applications. *Biosensors* **2022**, *12*, 500.

[40] Yang, S. H.; Zhu, J. J.; Lu, C. F.; Chai, Y.; Cao, Z.; Lu, J. J.; Zhang, Z.; Zhao, H.; Huang, Y. Y.; Yao, S. L. et al. Aligned fibrin/functionalized self-assembling peptide interpenetrating nanofiber hydrogel presenting multi-cues promotes peripheral nerve functional recovery. *Bioact. Mater.* **2022**, *8*, 529–544.

[41] Höke, A. A (heat) shock to the system promotes peripheral nerve regeneration. *J. Clin. Invest.* **2011**, *121*, 4231–4234.

[42] Zhang, H. Y.; Yin, F. F.; Shang, S.; Li, Y.; Qiu, Z. C.; Lin, Q. H.; Wei, X.; Li, S. L.; Kim, N. Y.; Shen, G. Z. A high-performance, biocompatible, and degradable piezoresistive-triboelectric hybrid device for cross-scale human activities monitoring and self-powered smart home system. *Nano Energy* **2022**, *102*, 107687.

[43] Won, D.; Kim, J.; Choi, J.; Kim, H.; Han, S.; Ha, I.; Bang, J.; Kim, K. K.; Lee, Y.; Kim, T. S. et al. Digital selective transformation and patterning of highly conductive hydrogel bioelectronics by laser-induced phase separation. *Sci. Adv.* **2022**, *8*, eabo3209.

[44] Yu, X.; Li, C.; Cui, J.; Feng, H.; Ding, Y. F.; Song, J. H.; Cai, P. F.; Chen, L.; EL-Newehy, M.; Abdulhameed, M. M. Advanced electroactive and anti-inflammatory sutures for enhancing tendon and bone regeneration to promote repair of achilles tendon sleeve avulsion. *Adv. Funct. Mater.* **2026**, *36*, e16062.

[45] Taniguchi, H.; Nagata, M.; Yano, H.; Okuzaki, H.; Takeoka, S. Evaluation of stability and cytotoxicity of self-doped PEDOT nanosheets in a quasi-biological environment for bioelectrodes. *ACS Appl. Polym. Mater.* **2024**, *6*, 1645–1652.

[46] Dong, X. H.; Liu, S. Y.; Yang, Y. Y.; Gao, S.; Li, W. L.; Cao, J. S.; Wan, Y.; Huang, Z. Q.; Fan, G. W.; Chen, Q. et al. Aligned microfiber-induced macrophage polarization to guide schwann-cell-enabled peripheral nerve regeneration. *Biomaterials* **2021**, *272*, 120767.

[47] Kim, G. B.; Chen, Y. J.; Kang, W. B.; Guo, J. S.; Payne, R.; Li, H.; Wei, Q.; Baker, J.; Dong, C.; Zhang, S. L. et al. The critical chemical and mechanical regulation of folic acid on neural engineering. *Biomaterials* **2018**, *178*, 504–516.

[48] Li, M. R.; Li, X.; Lv, Y. W.; Yan, H. D.; Wang, X. Y.; He, J.; Zhou, C.; Ouyang, Y. M. Chiral MoS_2@BC fibrous membranes selectively promote peripheral nerve regeneration. *J. Nanobiotechnology* **2024**, *22*, 337.

[49] Büttner, R.; Schulz, A.; Reuter, M.; Akula, A. K.; Mindos, T.; Carlstedt, A.; Riecken, L. B.; Baader, S. L.; Bauer, R.; Morrison, H. Inflammaging impairs peripheral nerve maintenance and regeneration. *Aging Cell* **2018**, *17*, e12833.

[50] Zheng, W. W.; Zhang, P.; Che, H.; Zhang, Y.; Yang, X.; Shen, Y. X. GsMTx4 ameliorates spinal cord injury by regulating microglial polarization through the Piezo1/NFκB/STAT6 pathway. *J. Neurorestoratol.* **2024**, *12*, 100144.

[51] Numata, T.; Tsutsumi, M.; Sato-Numata, K. Optogenetic and endogenous modulation of Ca^{2+} signaling in Schwann cells: Implications for autocrine and paracrine neurotrophic regulation. *Int. J. Mol. Sci.* **2025**, *26*, 9082.

[52] Christie, K. J.; Krishnan, A.; Martinez, J. A.; Purdy, K.; Singh, B.; Eaton, S.; Zochodne, D. Enhancing adult nerve regeneration through

the knockdown of retinoblastoma protein. *Nat. Commun.* **2014**, *5*, 3670.

[53] Rayner, M. L. D.; Healy, J.; Phillips, J. B. Repurposing small molecules to target PPAR-γ as new therapies for peripheral nerve injuries. *Biomolecules* **2021**, *11*, 1301.

[54] Zhou, Z. K.; Luo, G. J.; Li, C.; Zhang, P. Y.; Chen, W.; Li, X. X.; Tang, J. Y.; Qing, L. M. Metformin induces M2 polarization via AMPK/PGC-1α/PPAR-γ pathway to improve peripheral nerve regeneration. *Am. J. Transl. Res.* **2023**, *15*, 3778–3792.

[55] Teo, C. H. Y.; Lin, M. T. Y.; Lee, I. X. Y.; Koh, S. K.; Zhou, L.; Goh, D. S.; Choi, H.; Koh, H. W. L.; Lam, A. Y. R.; Lim, P. S. et al. Oral peroxisome proliferator-activated receptor-α agonist enhances corneal nerve regeneration in patients with type 2 diabetes. *Diabetes* **2023**, *72*, 932–946.

[56] Liu, C. L.; Zhang, H. J.; You, X. Y.; Cui, K. P.; Wang, X. C. Electrically conductive tough gelatin hydrogel. *Adv. Elect. Mater.* **2020**, *6*, 2000040.

[57] Hu, R. D.; Cao, Q. Y.; Sun, Z. Q.; Chen, J. Y.; Zheng, Q.; Xiao, F. A novel method of neural differentiation of PC12 cells by using Opti-MEM as a basic induction medium. *Int. J. Mol. Med.* **2018**, *41*, 195–201.

[58] Chen, S. F.; Zhou, Y. Q.; Chen, Y. R.; Gu, J. fastp: An ultra-fast all-in-one FASTQ preprocessor. *Bioinformatics* **2018**, *34*, i884–i890

[59] Kim, D.; Langmead, B.; Salzberg, S. L. HISAT: A fast spliced aligner with low memory requirements. *Nat. Methods* **2015**, *12*, 357–360.

[60] Pertea, M.; Pertea, G. M.; Antonescu, C. M.; Chang, T. C.; Mendell, J. T.; Salzberg, S. L. StringTie enables improved reconstruction of a transcriptome from RNA-seq reads. *Nat. Biotechnol.* **2015**, *33*, 290–295.

[61] Li, B.; Dewey, C. N. RSEM: Accurate transcript quantification from RNA-Seq data with or without a reference genome. *BMC Bioinformatics* **2011**, *12*, 323

[62] Love, M. I.; Huber, W.; Anders, S. Moderated estimation of fold change and dispersion for RNA-seq data with DESeq2. *Genome Biol.* **2014**, *15*, 550.

[63] Liberzon, A.; Birger, C.; Thorvaldsdóttir, H.; Ghandi, M.; Mesirov, J. P.; Tamayo, P. The Molecular Signatures Database (MSigDB) hallmark gene set collection. *Cell Syst.* **2015**, *1*, 417–425.